UiO : Department of Mathematics
University of Oslo

Investigating the Link Between Patient-specific Morphology and Hemodynamics: Implications for Aneurism Initiation?

Aslak Wigdahl Bergersen

Master's Thesis, Spring 2016

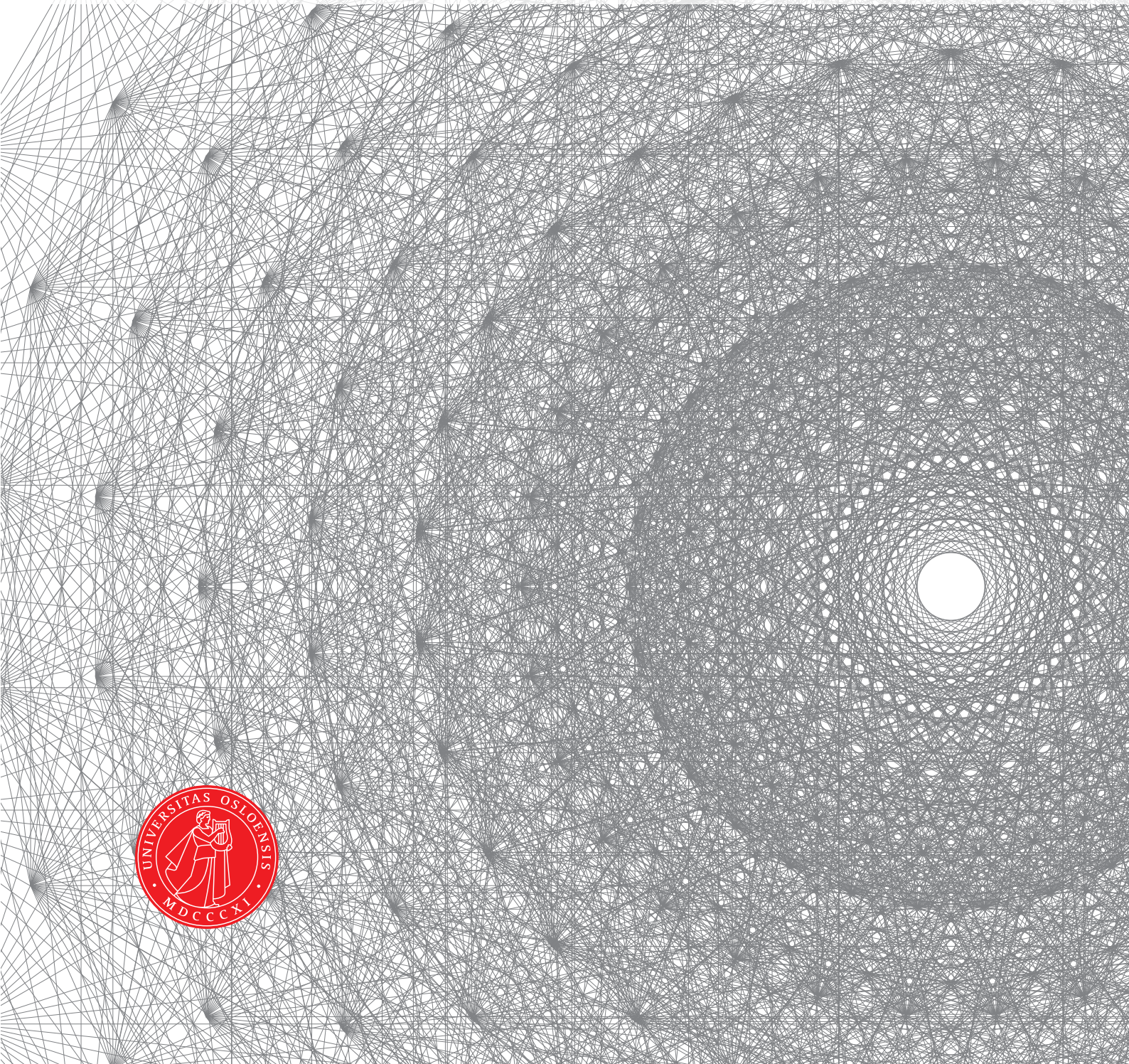

Cover design by Martin Helsø

The front page depicts a section of the root system of the exceptional Lie group E_8, projected into the plane. Lie groups were invented by the Norwegian mathematician Sophus Lie (1842–1899) to express symmetries in differential equations and today they play a central role in various parts of mathematics.

Contents

Abstract

Brain aneurysms are focalized diseased blood vessels, often shaped like a balloon, which can rupture and cause bleeding in the brain. The presence of aneurysms is correlated with internal carotid artery (ICA) extracranial area variations and wider angles in the intracranial ICA terminus bifurcation.

The goal of this thesis was to investigate a plausible hemodynamic stimulus that is statistically correlated with aneurysm presence by altering the morphological features in patient-specific geometries accordingly. The thesis is split into the following three chapters.

To trust the numerical results, we first validate the solver for biomedical flows by employing the U.S Food and Drug Administration's benchmark for an idealized medical device [Stewart et al. 2012 *Cardiovascular Engineering and Technology*]. We obtained different results compared to previous studies, but offering reasonable explanations to the observed discrepancies, we put faith in our numerical solution.

In the second chapter, a framework for objective manipulation of morphological features of intracranial arteries is presented and validated. As part of this work, an incremental improvement is made to the method for aneurysm removal presented in [Ford et al. 2009, *British journal of radiology*].

Finally, in the third chapter, we use the results from the previous two chapters to computationally investigate a plausible stimulus causing aneurysm initiation. Our results indicate that the plausible hemodynamic stimulus that statistically correlated with the presence of aneurysms is instable flow. That being said, in vitro/vivo studies are needed to confirm the mechanistic link between flow instabilities and the presence of aneurysms. Finally, we also present plausible explanations for why the leading theory of aneurysm initiation is an unlikely to occur in vivo.

Acknowledgements

Without the guidance, critic, and ideas from my main supervisor Dr. Kristian Valen-Sendstad, there would not have been any master thesis. I would like to extend my greatest gratitude for the time you have spent supervising me. You have always involved me in your brilliant thoughts and work, which has been a educational journey.

I would also like express my gratitude to Professor Mikael Mortensen and Dr. Martin Sandve Alnæs for being my co-supervisors. Simula and the BioComp department have provided me an excellent working environment during the work of this thesis.

Thanks to Professor David A. Steinman for sharing his brilliant mind and, hosting me for two months in the Biomedical Simulation Laboratory (BSL) at the University of Toronto, Canada. I would also like to thank the other members of the BSL, Dr. Diego Gallo, Mohammed Owais Khan, and Dr. Christopher Chnafa, for sharing their expertise.

I would like to thank my beautiful and brilliant girlfriend and partner, Chloé Beate Steen, for her love and support during the work of this thesis. You motivate me to always be the best version of my self.

Thanks to Remi, my brother from another mother, whom has acted as my trainer, life coach and physiatrist during my years at University.

Thanks to my mother, Preben, the rest of my family, and my friends, this thesis is dedicated to you.

Aslak W. Bergersen

Oslo, March 2016

Chapter 1

Introduction and Medical Background

Stroke is the second leading cause of death in the world, and accounted for over 12% of all deaths (6.4 million) in 2013 [1]. Stroke is a term for describing any incident that may cause reduced blood flow to the brain. Stroke and cardiovascular diseases are in general burdening the healthcare systems, and the costs are expected to rise in the years to come due to longer life expectancy and unhealthy lifestyle [2]. Although the mortality rate of stroke has been reduced worldwide by one fifth since 1990 [1], there are still major challenges to fully understand the disease initiation and progression [3].

One type of stroke is caused by bleeding into the space between the brain and the scull. This is called a subarachnoid hemorrhage, and is the cause of 5% of all strokes [4]. It is most commonly caused by an aneurysm rupture (85%) [4, 5]. An aneurysm is a balloon-shaped bleb on a the blood vessel, and the wall is more brittle and less compliant than the rest of the vasculature, see Figure 1.1A [6]. Aneurysms are located in bifurcations at the base of the brain in vicinity of, or on, Circle of Willis [4]. In contrast to other types of strokes, subarachnoid hemorrhage often strikes at relatively young age, with median age of 55 years [7, 8, 9, 3]. Approximately 27% years of potential life lost from stroke before age 65 is caused by aneurysms [8]. In addition, the mortality rate after a subarachnoid hemorrhage is 50%, and of positive outcomes only 25% of the survivors report full recovery without any psychosocial or neurological problems [10]. Of equal importance is the great personal tragedy of those affected. This leaves no doubt that basic research into aneurysms is needed. Interdisciplinary basic research could have a significant socioeconomic impact, decrease the mortality rate, and give increased recovery for the survivors.

The entire cardiovascular system is constantly undergoing remodeling to

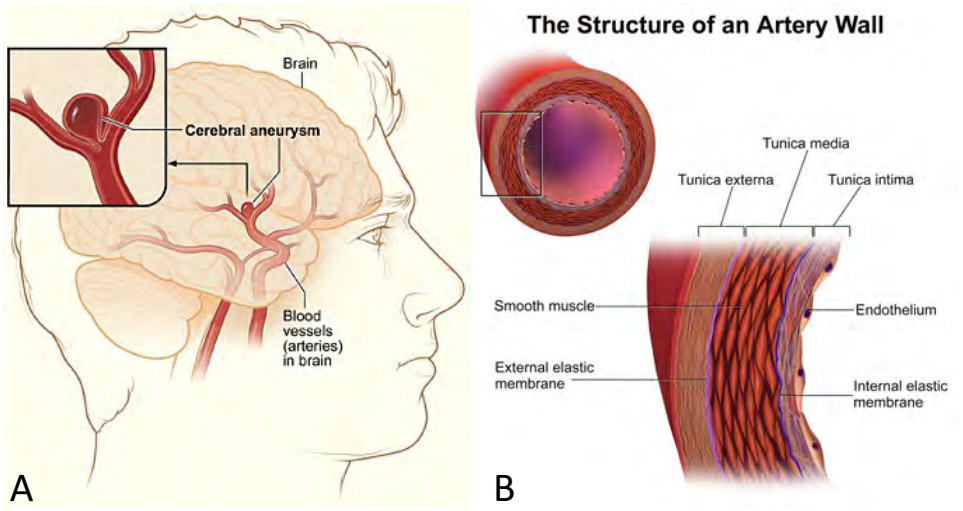

Figure 1.1: **A** Illustration of an aneurysm located in the middle communicating artery (Wikipedia Commons / Public Domain). **B** View of each layer in the blood vessel. (Blausen.com staff. Wikiversity Journal of Medicine. DOI:10.15347/wjm/2014.010. ISSN 20018762.)

adapt to the local blood flow. Remodeling is controlled by the endothelial cells, which covers the inside wall of the blood vessel, see Figure 1.1B. On each endothelial cell there are receptors which react to the wall shear stress (WSS) caused by the flow of blood. The mechanics of blood flow is called hemodynamics. Depending on the hemodynamic forces acting on the cell, it produces substances which will contract or relax the smooth muscle cells in the tunica media, see Figure 1.1B. This process is called mechanotransduction, and describes a mechanical stimuli converted into electrochemical activity. It is commonly accepted that aneurysms are formed when the blood vessel walls undergo adverse remodeling due to an abnormal hemodynamic environment. Scientists have therefore spent a large amount of resources to find the hemodynamic stimuli associated with aneurysm rupture and initiation. In collaboration with vascular biologists we could find the mechanobiology that cause the disease. This knowledge might provide us with an improved understanding of the pathology and physiology (pathophysiology) of aneurysms and lead to improved treatments and preventive measures.

The local hemodynamic of intracranial aneurysms is challenging to measure. However, high-resolution medical images are available, and have in combination with computational fluid dynamics (CFD) been extensively used as a surrogate to study the plausible patient-specific forces acting on the blood vessel wall [11]. From such retrospective CFD studies, aneurysm rupture is believed to be caused by complex and unstable flow patterns [12]. This

is further supported by large cohort studies from Cebral et al. (2011) with 210 patients, and Xiang et al. (2011) with 119 patients, which both found rupture to be associated with a complex flow [13, 14]. However, aneurysm initiation is believed to be caused by a combination of high WSS and WSS gradients (WSSG) [15]. This hypothesis was put forth based on a set of experiments in rabbits and canines. With a surgical procedure, the flow rates were increased to induce aneurysm initiation, see Figure 1.2A and B for an example. In the study from Metaxa et al. (2010), this caused the flow rates to increase on average by 325% and cause aneurysm initiation in the test subjects [16]. Based on the CFD simulations on the subject specific geometries, see Figure 1.2C and D, the authors concluded that the combination of WSS and WSSG is a dangerous stimulus causing aneurysm initiation [16, 15, 17, 18, 19]. This is currently the only theory addressing what kind of hemodynamic stimuli can cause aneurysm initiation.

Controversial results reported by Valen-Sendstad et al. (2013, 2014a, and 2014b) showed that the flow in the carotid siphon can be unstable in some patients, and challenged the validity of previous results [20, 21, 22]. In textbooks and previously published articles blood flow is reported to be laminar. However, Valen-Sendstad et al. (2013) hypothesized that the flow might be unstable due to large area variation and curvature as the vessels penetrate the scull. Instead of assuming anything about the flow, they followed best-practice guidelines for CFD [23]. First of all, they started with a second order accurate solver in time and space, the same as described in Chapter 2. Then, they performed a convergence study in both time and space until they found a mesh independent solution [20]. The results and follow-up studies have shown that the combination of solvers, time steps, and mesh resolution normally applied in the literature are insufficient to detect flow instabilities [21, 24]. In a study from Valen-Sendstad et al. (2014b), it has further been hypothesized that the stimulus from flow instabilities might be the cause of aneurysm initiation [20]. In light of these results, previous established truths, such as high WSS and WSSG being the cause of aneurysm initiation, have to be reexamined.

This thesis has two main goals: 1) **evaluate the validity of high WSS and WSSG being the cause of aneurysm initiation**, and 2) **investigate if a fluctuating flow can be a plausible stimuli for aneurysm initiation.**

The approach to reach these goals is to look at what we know about aneurysm initiation. From previous studies, we know that there are at least four morphological features of the internal carotid artery (ICA) that are statistically correlated with the presence of aneurysm: winder angles in the ICA terminus bifurcation [25, 26], increased area variations of the ICA [27], high peak curvature in ICA [28], narrow angle of the bend in the ICA siphon [29],

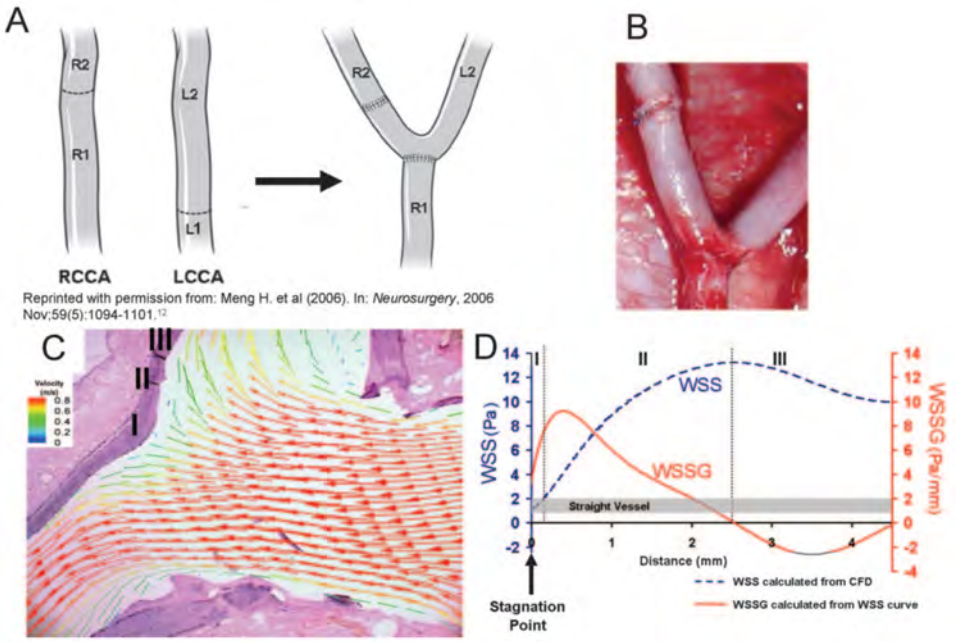

Figure 1.2: Illustration taken from Meng et al. (2007) with the original caption: "**A**, Schematic of bifurcation creation. L (R)-CCA indicates left (right) common carotid artery. **B**, A created bifurcation. **C**, Overlay of CFD-calculated velocity vectors (color indicates magnitude) on a histologic section of a bifurcation (from dog No. 4) 2 months after creation (van Gieson's staining). **D**, WSS and WSSG along the median wall of the bifurcation apex (left branch) reveal 3 regions with distinct flow characteristics: I, the impingement region; II, acceleration region; and III, recovery region. The range of normal physiologic WSS values for a straight vessel segment is indicated by the gray band." [15]

and large torsion in the ICA [30]. If each morphological feature could be modified in patient-specific geometries, then we could investigate how the hemodynamic stimuli changes. From a logical point of view, the observed hemodynamic stimuli should be correlated with aneurysm initiation. Therefore, the idea of this thesis is to use a *validated* solver for biomedical applications to investigate the *link between morphology and hemodynamic stimuli* in *patient-specific geometries*.

To achieve the goals of this thesis, it is split into three separate studies: *Verification and Validation* of the solver, *An Objective Approach for Manipulating Morphological Features in Arteries*, and *A Computational Study of the Link Between Hemodynamics and Morphology in the Internal Carotid Artery*. Each part is designed as a complete study with a method, result, discussion, and conclusion section. In addition, the governing equations will

be briefly addressed. Finally, to summarize and discuss the 'big picture', a final discussion and conclusion will follow after the three studies.

The first part is *Verification and Validation*, and is presented in Chapter 3. Following best-practices CFD guidelines, the solver is validated for the intended application. Therefore, a well documented benchmark is chosen and simulated. The results were far more complex then anticipated, and therefore this chapter is more extensive than a normal validation case. However, it illustrates the importance of proper *verification and validation* and is necessary for the validity of the rest of the numerical results.

The second part is *An Objective Approach for Manipulating Morphological Parameters in Arteries*. To the author's best of knowledge, there is no method for objective manipulation of patient-specific morphology in the parent artery presented in the literature. The second part is to create a framework of tools needed to test the hypothesis of aneurysm initiation, and is presented in Chapter 4. Only the two first geometrical features will be addressed, namely angle in the ICA terminus and area variations of the ICA .

The third and final part is *A Computational Link Between Morphology and Hemodynamic*. We here investigate patient-specific geometries of healthy patients and vary the morphological features to shed light on the hemodynamic stimuli associated with aneurysm initiation.

At the time of writing, results from this thesis have been published in a national conference in Computational Mechanics as one refereed proceeding and presented as a talk. In addition, three peer-reviewed proceedings have been accepted, and one has been submitted to two international conferences.

Bø J, **Bergersen AW**, Valen-Sendstad K, Mortensen M. Implementation, validation and verification of large eddy simulation models in Oasis. In MekIt'15: 8. National Conference on Computational Mechanics, May 2015, Trondheim, Norway. *Refereed proceeding and contributed talk.*

Bergersen AW, Jiménez JM, Valen-Sendstad K. Can Manipulation of Arterial Morphology Shed Light on the Mechanobiological Stimuli Behind Aneurysm Initiation? 11th International Symposium on Biomechanics in Vascular Biology and Cardiovascular Disease, May 2016, Atlanta, U.S.A. (*Accepted for podium presentation*)

Bergersen AW, Chnafa C, Gallo D, Piccinelli M, Valen-Sendstad K. An Objective Approach for Digital Removal of Bifurcation Aneurysms: Incremental Improvements? 11th International Symposium on Biomechanics in Vascular Biology and Cardiovascular Disease, May 2016, Atlanta, U.S.A. (*Accepted*)

Bergersen AW, Valen-Sendstad K. A Benchmark Standard Model of a

Generic Medical Device; All Models Are Wrong, but Some Are Useful. 11th International Symposium on Biomechanics in Vascular Biology and Cardiovascular Disease, May 2016, Atlanta, U.S.A. (*Accepted*)

Bergersen AW, Mortensen M, Valen-Sendstad K. The FDA's Nozzle Benchmark: In Theory, There Is No Difference Between Theory and Practice. But, in Practice, There Is. Summer Biomechanics, Bioengineering, and Biotransport Conference, June 2016, Maryland, U.S.A. (Submited)

Chapter 2

Governing Equations

The Navier-Stokes equations [31] describe fluid motion, and are derived using conservation of mass and momentum. In the form stated in this thesis (2.1)-(2.2) we assume an incompressible Newtonian fluid, i.e., constant density (ρ) and dynamic viscosity (μ). The Navier-Stokes equations can then be written as

$$\frac{\partial u}{\partial t} + u \cdot \nabla u = -\frac{1}{\rho}\nabla p + \frac{\mu}{\rho}\nabla^2 u + f \tag{2.1}$$

$$\nabla \cdot u = 0 \tag{2.2}$$

where p is the pressure, u is the velocity, and f is a body force. Existence or smoothness for Navier-Stokes is not proven, i.e., it is not proven that Navier-Stokes has a mathematical solution. This is one of the seven millennium problems with a prize of one million dollars [32]. Nevertheless, numerical simulations are consistent with experiments, and have been applied in a wide range of applications [33].

Previous numerical studies have shown that for blood flow in intracranial arteries, the combination of discretisation, number of time steps, and mesh resolution has a large impact on the computed hemodynamic environment [21, 24]. In particular, lower order solvers with low spatial and temporal resolution are not able to capture instabilities and fluctuations in the flow. From the study by Khan et al. (2015), we know that the open-source solver *Oasis* [34] performed well with regards to capturing transition in the intended application [24]. Therefore *Oasis* will be used for all flow simulations in this thesis.

There are multiple numerical schemes implemented in *Oasis*, but the one used here is a *fractional step* method. The general idea of *fractional step*

methods is to split the original equations (2.1)-(2.2) into smaller well studied problems. A general fractional step method with second order accuracy in time can be written [35]

$$\frac{u_k^\star - u_k^{n-1}}{\Delta t} + B_k^{n-1/2} = -\nabla_k p^\star + \nu \nabla^2 u_k^{n-1/2} + f_k^{n-1/2} \qquad \text{for } k = 0, \ldots, d \tag{2.3}$$

$$\nabla^2 \varphi = \frac{1}{\Delta t} \nabla \cdot \boldsymbol{u}^\star \tag{2.4}$$

$$\frac{u_k^n - u_k^\star}{\Delta t} = -\nabla_k \varphi \qquad \text{for } k = 0, \ldots, d \tag{2.5}$$

where $p^\star$ and $u^\star$ are the tentative pressure and velocity, $\varphi = p^{n-1/2} - p^\star$, $B_k = \boldsymbol{u} \cdot \nabla u_k$ is the convective term, the superscript n is for time, d is the number of spatial dimensions, and Δt is the time step. A variable change has been made for the pressure, $p = \frac{1}{\rho}\tilde{p}$, where $\tilde{p}$ is the physical pressure in equation (2.1). In equation (2.3)-(2.5) the unknowns are the tentative velocity $u^\star$, pressure $p^{n-1/2}$ and the velocity u^n, respectivly. This implies that the discrete velocity and pressure solutions are defined on different time steps.

The temporal discretization of the convective term ($B^{n-1/2}$) and viscous term ($\nu \nabla^2 u^{n-1/2}$) still needs to be addressed. To that end the convective term is first linearized by an Adam-Bashforth projection of the convecting velocity $\boldsymbol{u}^{n-1/2} \cdot \nabla u^{n-1/2} = (1.5\boldsymbol{u}^{n-1} - 0.5\boldsymbol{u}^{n-2}) \cdot \nabla u^{n-1/2}$. The Adam-Bashforth linearization makes the solution energy conservative, and minimal diffusive. To avoid strict restrictions on the time step (Δt), and keep the second order accuracy in time, a Crank–Nicolson discretization is chosen for both terms $u_k^{n-1/2} = 0.5(u_k^\star + u_k^{n-1})$.

Following Algorithm 1, an initial guess for the tentative pressure is first made using the previous time step. Then equation (2.3) is solved with respect to the tentative velocity. At this point there is no guarantee that $u_\star$ is divergence free. Therefore, the pressure is projected onto a divergence free velocity space. Equations (2.3)-(2.4) can be solved iteratively until a criteria on either desired accuracy or maximum number of iterations is satisfied. The tentative velocity and the pressure at $n - 1/2$ is then used to find the velocity at the next time step u^n. This is repeated for each time step until $t = T$. The solver is second order in time and $m + 1$ in space, where m is the polynomial degree of the element [35], this is also confirmed by a order-of-convergence test in Section 3.1.

A drawback with the *fractional step* scheme is that the boundary condition

Algorithm 1: A generic fractional step method, the algorithm is rewritten following Mortensen et al. [34].

Set initial condition
t = 0
while $t < T$ **do**
    t = t + dt
    while *error* < *max_error* **and** *iter* < *max_iter* **do**
        $\varphi = p^\star = p^{n-1/2}$
        solve (2.3) for $u_k^\star$ for $k = 0, \ldots, d$
        solve (2.4) for $p^{n-1/2}$
    $\varphi = p^{n-1/2} - \varphi$
    solve (2.5) for u_k^n for $k = 0, \ldots, d$
    update to next time step

for the pressure is not a natural part of the new equations, however there are suggested solutions to this problem [36]. Another aspect of the fractional step method is that the new equations are separately well studied problems and can be solved with control on the accuracy, stability, and efficiency. However, we do not know how well the overall solution algorithm behaves [37]. Nevertheless, studies have reported that multiple *fractional step* schemes are in agreement with experiments and show theoretical convergence towards exact solutions [36].

Mortensen et al. reported that roughly 75% of the computational time was spent inside highly efficient Krylov solvers, and much of the remaining time is used to assemble the coefficient matrix. This arguably makes it an efficient method limited by the linear solver provided by PETSc, a third party state of the art linear algebra backend solver. Furthermore, as a built-in function in FEniCS the code also runs in parallel without any additional effort. Mortensen et al. reported that the solver scales weakly up to 256 CPUs on the Abel super computer cluster [34].

Chapter 3

Verification and Validation

The use of scientific computing has increased tremendously the past decades, and has a profound impact in both industry and academia. Scientific computing reduces the time and cost spent on prototyping and testing compared to experimental approach [38]. However, blind faith in computational results has caused major accidents. One example is the *Sleipner A* oil platform that sank outside the coast of Norway in 1991. Nobody was killed in the accident, but the total loss amounted to $700 million at the time. The accident was caused by a mistake in the numerical computation of the shear stress in the concrete of the gravity base structure. The mistake would most likely have been detected, and the accident prevented, if *validation and verification* of the numerical methods had been performed [39]. In general, the framework of *verification and validation* is used to check if the numerical solution is accurate and realistic enough to describe the real life problem.

The process of describing a real-life problem with numerical experiments can be divided into three parts: describing the problem mathematically, solving the mathematical problem numerically, and use the solution to answer the original question. To ensure that the solution can be trusted we have to know if the problem is described with the correct equation, and that the equation is implemented and solved correctly. Simplified, *verification* is to check if the implementation is correct, and *validation* is to check if the correct equation is solved. This implies that *verification* always has to be performed before *validation*. In the literature of *verification and validation*, *verification* is further split into two groups: *verification of code* and *verification of solution* [40]. *Verification of code* is to check if the equation is implemented correctly, and *verification of solution* is to check the input data, account for all errors in the computation, and verify post-processing of the solution. Addressing these three categories can not guarantee that all mistakes are found or that the model is perfect, however we do know

that some specific types of errors are excluded. In addition, one also has an estimate of how accurate the model is. This could be summed up with the elegantly formulated quote from Edsger W. Dijkstra: *"Program testing can be a very effective way to show the presence of bugs, but is hopelessly inadequate for showing their absence"* [41].

Thus, an important part of the definition of *verification and validation* is that it is a continuous process without a definite end. For *verification of code* this may no longer be true. To compare the strength of *verification of code* tests, Knupp and Salari (2002) implemented coding mistakes in a working and error-free script. Using the new script with errors, a blinded user performed *verification of code* tests to check which mistakes were detected. Using the *method of manufactured solution*, described in detail below, they found that all mistakes affecting the accuracy of the solution, except one, were detected [42]. However, Roach (2002) pointed out that if the test is performed according to his guidelines [43], the final mistake would have been detected. From this, Roach concluded that *verification of code* in fact has a final goal, i.e. to pass a *method of manufactured solution* test [44].

The goal of this chapter is to performe *verification and validation* of the *Oasis* solver [34]. The *verification of code* will be addressed using the *method of manufactured solution*. *Verification of solution* will not be reported, but has been performed. Finally *validation* of the solver will be done against a well documented benchmark, presented in Section 3.2. *Verification and validation* of the boundary conditions applied for intracranial blood flow is beyond the scope of this thesis. Model validation is not addressed in this thesis, but model assumptions/limitations for blood flow simulation in intracranial arteries are discussed in Chapter 5.

3.1 Verification of Code

Verification of code has multiple approaches, but the most rigorous way is to do order-of-convergence tests [38]. The idea of an order-of-convergence test is to compare the numerical solution to an analytical (or highly accurate) solution and observe the rate of convergence when spatial or temporal discretization is refined. The test is considered passed if the observed order of convergence matches the theoretical convergence. Order-of-convergence tests can be separated into four groups depending on how the analytical (or highly accurate) solution is obtained. The most rigorous of these is *method of manufactured solutions* (MMS) [38], which is the choice of method for *verification of code* in this thesis.

To explain the idea of MMS, we consider a general differential equation on the following form

$$\mathcal{L}(u) = f \tag{3.1}$$

where $\mathcal{L}$ is some differential operator, u is the unknown, and f is a known source term. The normal approach for solving this equation is, given a known f, to invert $\mathcal{L}$, and solve for u. In MMS the equation is not solved, but a carefully chosen solution u is manufactured. The f corresponding to the manufactured solution is found by computing $\mathcal{L}(u)$, and is then provided as input for the solver to obtain the numerical solution. The numerical solution can then be compared to the manufactured solution in an order-of-convergence test.

There are multiple rules for how to perform a MMS test. For the incompressible Navier-Stokes equation, the rules can be summed up by these four points [38, 42, 44]:

1. All functions have to be analytical and sufficiently smooth.

2. The chosen solution has to be complex enough that each term in (2.1) is non-zero and no term in equation (3.1) should dominate other terms [38], i.e., the Reynolds number should be around unity such that the convective and diffusive terms are of the same order of magnitude.

3. The solution should not be strongly varying in time and space, i.e. include a small constant term. This also implies that the solution should not include singularities.

4. Solution must be admissible, i.e., adhering to all constraints in the system of equations.

In addition to these rules, two best-practice guidelines are also applied during this test. *First*, the initial condition is set to be the exact solution rather than zero [44]. *Second*, the exact solution is applied as a Dirichlet boundary condition, at the entire boundary for both u and p. Although the problem is now mathematically overdetermined and ill-posed, this should not affect the observed convergence in the test, as discussed by Oberkampf (2010) [38].

Following the rules and best-practice guidelines listed above, a carefully chosen manufactured solution is found. To meet the criteria for smoothness, trigonometric functions such as sine and cosine are a good choice. The fourth rule is addressed by letting the velocity component w be computed from u and v to ensure that the solution is divergence free. The manufactured solution chosen for the 3D incompressible Navier-Stokes is

$$u = u_0(\sin(\pi(x+y+z)) + \cos(\pi yz))\sin(t) + \epsilon \tag{3.2}$$

$$v = v_0(-\cos(\pi(x+y+z)) + \cos(\pi xz))\sin(t) + \epsilon \tag{3.3}$$

$$w = -w_0 \int \frac{\partial u}{\partial x} + \frac{\partial v}{\partial y}\, dz + \cos(\pi xy) + \epsilon \tag{3.4}$$

$$= w_0(v_0 \cos(\pi(x+y+z)) - u_0 \sin(\pi(x+y+z)))\sin(t) + \cos(\pi xy) + \epsilon \tag{3.5}$$

$$p = \tanh(x^2+y^2+z^2)\cos(t) + \epsilon \tag{3.6}$$

where $u_0 = 1.5$, $v_0 = 1.2$, $w_0 = 0.4$, $\epsilon = 0.05$. To ensure a Reynolds number around unity the kinematic viscosity is set to $\nu = 4$. The computational domain is an unit cube, and the simulation for the spatial convergence is stopped at $t = 0.01$ s. Since the temporal convergence study includes larger time steps, the simulations are stopped at $t = 10.0$. It is the error in the last time step that is used to compute the error. The corresponding f of the solution is automatically computed using SymPy [45], but not reported since it is a lengthy expression. The method for computing f can be found in *find_f.py* in [46], and can be considered a general approach for finding f in FEniCS as it can easily be modified to other equations.

To compute the error, the exact solution is represented on a finer mesh with elements of higher polynomial degree. The numerical solution is projected onto the same mesh as the exact solution to compute the error. The error of the representation in the exact solution is then negligible compared to the numerical error. Let u be the numerical solution, and u_e the exact solution, then the error E is computed as

$$E = \frac{||u - u_e||}{||u_e||} \tag{3.7}$$

where $||\cdot||$ is the L^2-norm. Now, assuming that the tetrahedrons are perfect with $\Delta x = \Delta y = \Delta z$, and a constant time step Δt, then the error can be expressed as

$$E = C\Delta x^k + D\Delta t^l \tag{3.8}$$

where C, and D are constants. From Chapter 2 we recall that the expectation is $l = 2$ and $k = m + 1$, where m is the polynomial degree of the elements. To find the rates of convergence in time (l) the contribution from the spatial discretization has to be negligible while Δt is studied, and vice

N	Δt	m	E_u	k_u	E_p	k_p
16	$1.00 \cdot 10^{-6}$	1	$2.26 \cdot 10^{-7}$	-	$1.09 \cdot 10^{-4}$	-
32	$1.00 \cdot 10^{-6}$	1	$5.86 \cdot 10^{-8}$	**1.95**	$3.04 \cdot 10^{-5}$	**1.96**
64	$1.00 \cdot 10^{-6}$	1	$1.48 \cdot 10^{-8}$	**1.98**	$7.84 \cdot 10^{-6}$	**1.96**
128	$1.00 \cdot 10^{-6}$	1	$3.71 \cdot 10^{-9}$	**2.00**	$1.96 \cdot 10^{-6}$	**2.00**
8	$1.00 \cdot 10^{-6}$	**2**	$1.52 \cdot 10^{-6}$	-	$2.64 \cdot 10^{-4}$	-
16	$1.00 \cdot 10^{-6}$	**2**	$2.09 \cdot 10^{-7}$	**2.86**	$3.45 \cdot 10^{-5}$	**2.94**
32	$1.00 \cdot 10^{-6}$	**2**	$2.72 \cdot 10^{-8}$	**2.94**	$4.38 \cdot 10^{-6}$	**2.98**
64	$1.00 \cdot 10^{-6}$	**2**	$3.40 \cdot 10^{-9}$	**3.00**	$5.51 \cdot 10^{-7}$	**2.99**
64	$\mathbf{1.00 \cdot 10^{-1}}$	1	$5.14 \cdot 10^{-2}$	-	$4.95 \cdot 10^{-1}$	-
64	$\mathbf{5.00 \cdot 10^{-2}}$	1	$1.31 \cdot 10^{-2}$	**1.97**	$1.34 \cdot 10^{-1}$	**1.89**
64	$\mathbf{2.50 \cdot 10^{-2}}$	1	$3.29 \cdot 10^{-3}$	**1.99**	$3.37 \cdot 10^{-2}$	**1.99**
64	$\mathbf{1.25 \cdot 10^{-2}}$	1	$8.23 \cdot 10^{-4}$	**1.99**	$8.42 \cdot 10^{-3}$	**2.00**

Table 3.1: Results of the *method of manufactured solution* test. N is the number of elements on each side of the unit cube, the total number of cells are $6N^3$. Δt is the time step, and m is the polynomial degree of the elements. Both temporal and spatial observed convergence rates are in perfect agreement with the theoretical convergence rates.

versa for the spatial convergence rate. Let Δt^l be negligible in comparison with Δx^k and E_1 be the error on a coarse mesh and E_2 on a finer mesh, k is then found by

$$\begin{aligned} \frac{E_1}{E_2} &= \left(\frac{\Delta x_1}{\Delta x_2}\right)^k \\ \log\left(\frac{E_1}{E_2}\right) &= k \log\left(\frac{\Delta x_1}{\Delta x_2}\right) \\ k &= \frac{\log\left(\frac{E_1}{E_2}\right)}{\log\left(\frac{\Delta x_1}{\Delta x_2}\right)} \end{aligned} \tag{3.9}$$

The results are presented in Table 3.1, and show convergence towards the expected theoretical values. For comparison, Mortensen et al. (2015) reported 4th order convergence with second order elements using Taylor-Green vortex in 2D [34]. This is superconvergence and is due to a perfect mesh aligned with the axis and periodic boundary conditions [47]. The convergence would drop to 3rd order for an unstructured mesh. Thus, these results are not contradicting and this version of the code could be considered verified.

3.2 Validation

A general strategy for validation is to compare the numerical solution of the simulation with experimental results to check if the model is sufficiently accurate for the intended application. Accurate experimental measurements of complex multiphysics problems are difficult to obtain, and biomedical flows are no exception. Therefore, a *building block* approach with a hierarchy of validation tests has been developed [48, 49]. The idea is to split the complete system into simpler cases with more accurate experiments for comparison. The method is then to start at the simplest possible problem, and then gradually increase in complexity and similarity towards the application of interest [38, 50, 48]. Previous validation studies of the solver have been performed by Mortensen et al. (2015) with turbulent channel flow [34] and by Valen-Sendstad et al. (in preparation) with a Taylor-Green vortex in 3D [51]. Taylor-Green vortex develops from an initial state of laminar flow to fully isotropic turbulence and then laminar again. Consequently, Taylor-Green is a good benchmark for capturing transition, which is an important property for the application of interest [21].

From the previous validation, we can state that the solver is validated for channel flow and transitional flow. Since blood flow in arteries essentially is transitional flow in a pipe, an appropriate next validation test should address both problems. In addition, it should also include one or more of the following: blood flow, pulsatile flow, or a more complex geometry. It is also positive if the validation test has proven to fail or be challenging for some models. A validation case fulfilling the listed criteria is the benchmark launched by the U.S. Food and Drug Administration (FDA) on an idealized medical device. The problem includes laminar, transitional and turbulent flow, and has a more complex geometry [52]. The benchmark has proven to be challenging, and as a result there have been four non-blind retrospective studies [53, 54, 55, 52, 56]. In conclusion, the FDA benchmark is a perfect next step in the current validation process of the solver towards the use in biomedical flows.

3.2.1 Method

The original study was designed as a blind challenge where the participants performed CFD simulations. The goal for this study was to *"(..) assess the current state of the art in CFD modeling with respect to predicting fluid dynamics in an idealized medical device model"* [52]. The problem set-up is flow through a pipe followed by a nozzle into a narrower cylinder leading to a sudden expansion, as illustrated in Figure 3.1. Only the geometry (Figure 3.1), flow rates (Table 3.2), and fluid property ($\nu = 3.31 \cdot 10^{-6}$)

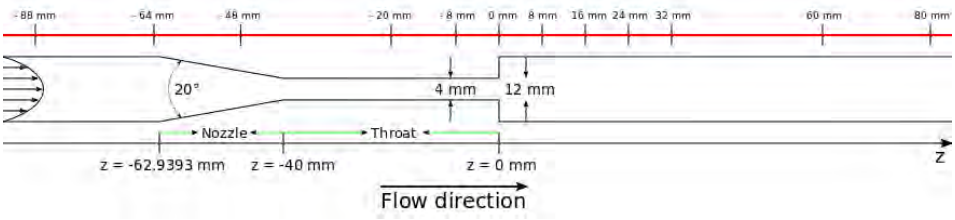

Figure 3.1: Geometry of the provided idealized medical device. The red line indicates slices where the participants were asked to provide statistics.

Re number at throat	Flow rate (m^3/s)
500	$5.21 \cdot 10^{-6}$
2000	$2.08 \cdot 10^{-5}$
3500	$3.64 \cdot 10^{-5}$
5000	$5.21 \cdot 10^{-5}$
6000	$6.77 \cdot 10^{-5}$

Table 3.2: List of flow rates for all experiments.

were available for the 28 participants of the blind study. As indicated by Table 3.2, there was one flow in the laminar regime ($Re = 500$), two flows in the transitional regime ($Re = 2000, 3500$), and two flows in the turbulent regime ($Re = 5000, 6500$).

The laminar and turbulent cases obtained the best agreement in the challenge. For the $Re = 3500$, none of the participants provided an accurate simulation that matched the experimental results, see Figure 3.2 [52]. The $Re = 3500$ flow will therefore be the main focus of this study. Following the best-practice guidelines for computational fluid dynamics, a refinement study in time and space will be performed for this case [23]. The rest of the cases will also be simulated, see Table 3.3 for a list of simulations. From this point on, the simulations will be referred to according to their Reynolds number and the mesh size. The notation for the elements are now PX-PY, where X and Y are the polynomial degree of the velocity and pressure, respectively.

The numerical results are compared to those obtained from experiments conducted at three independent laboratories. One of the laboratories conducted the experiment three times, resulting in five sets of experimental data in total. The results are obtained from particle image velocimetry (PIV) measurements, and the first time an interlaboratory PIV study has been performed for a medical problem. For more details regarding the experimental set-up, see Hariharan et al. (2011) [57].

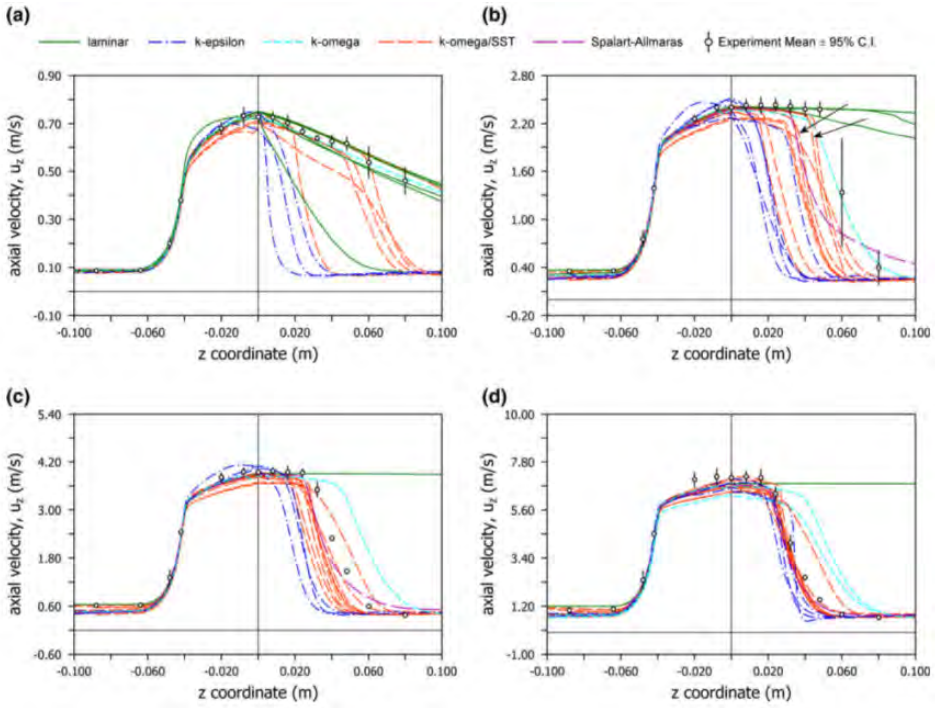

Figure 3.2: Results from the original FDA challenge. The figure is taken from Stewart et al. (2012), with the original caption: "*Axial velocity along nozzle centerline for throat Reynolds number = (a) 500, (b) 2000, (c) 3500, (d) 6500. Lines are CFD results plotted against turbulence model used (simulations with conservation of mass errors >10% are omitted). Arrows indicate SST transitional flow option used at Re* = 2000 *(not easily visible at other two Re). Symbols are interpolated experimental means* ±95% *CI.*" [52]

In the experimental set-up, the inlet pipe was 1.2 m long, and the exit pipe was 1.0 m. For the numerical simulations the computational domain is chosen to be 320 mm long, from $z = -120$ mm to $z = 200$ mm, which is the same as 26.7 diameters of the inlet. This is in agreement with previous studies [56], and the length of the inlet pipe does not affect the simulations. Meshes are created in ICEM-CFD (Ansys Inc., Canonsburg, PA, USA) by first creating a surface mesh using Octree method. This mesh is then smoothed using both Laplace and regular smoothing. From this surface mesh, the volume mesh is computed using Delaunay advancing front method with 4 boundary layers. The entire mesh is then smoothed again, except for the boundary layers. The mesh is then exported to ANSYS Fluent format (.msh) and converted to FEniCS mesh format (.xml) using a converting tool developed by Mikael Mortensen at the University of Oslo [58]. The workflow can be found in detail in [46]. To ensure reproducibility, the meshes are created with a uniform approach. In total, 4 meshes were produced with 5, 10, 17

	Mesh	Re at throat	Elements	dt
Space	**5M**	3500	P1-P1	$1 \cdot 10^{-5}$
	10M	3500	P1-P1	$1 \cdot 10^{-5}$
	17M	3500	P1-P1	$1 \cdot 10^{-5}$
	28M	3500	P1-P1	$1 \cdot 10^{-5}$
	10M	3500	**P2-P1**	$\mathbf{5 \cdot 10^{-6}}$
Time	17M	3500	P1-P1	$\mathbf{1 \cdot 10^{-5}}$
	17M	3500	P1-P1	$\mathbf{5 \cdot 10^{-5}}$
	17M	3500	P1-P1	$\mathbf{1 \cdot 10^{-4}}$
	17M	3500	P1-P1	$\mathbf{1.5 \cdot 10^{-4}}$
All Reynolds numbers	17M	**500**	P1-P1	$2 \cdot 10^{-5}$
	17M	**2000**	P1-P1	$1 \cdot 10^{-5}$
	17M	**3500**	P1-P1	$1 \cdot 10^{-5}$
	17M	**5000**	P1-P1	$5 \cdot 10^{-6}$
	17M	**6500**	P1-P1	$5 \cdot 10^{-6}$

Table 3.3: List simulation for this study. The first block is the refinement study in space, the second is refinement in time and the third is all Reynolds numbers simulated with the 17M mesh. The 17M-3500-P1-P1-$1 \cdot 10^{-5}$ simulation is presented in all categories, but is only simulated once. Approximately 350 000 CPU hours have been used in total on the Abel high performance computer cluster. This includes post-processing, and simulations that are not reported here.

and 28 million cells. These are now referred to as the 5M, 10M, 17M and 28M mesh, respectively. A view of the meshes at the sudden expansion is shown Figure 3.3. The color corresponds to the characteristic cell length defined as

$$\Delta x = \sqrt[3]{6\sqrt{2}\Delta_{vol}} \tag{3.10}$$

where Δ_{vol} is the volume of a cell.

The dimensionless Courant number is introduced as an indicator of how resolved in time the problem is. It is defined as

$$C = \frac{\Delta t}{\Delta x}(u_x + u_y + u_z) \tag{3.11}$$

assuming Δx is equal in all directions. The Courant number is also used as stability criteria referred to as Courant–Friedrichs–Lewy condition, and for

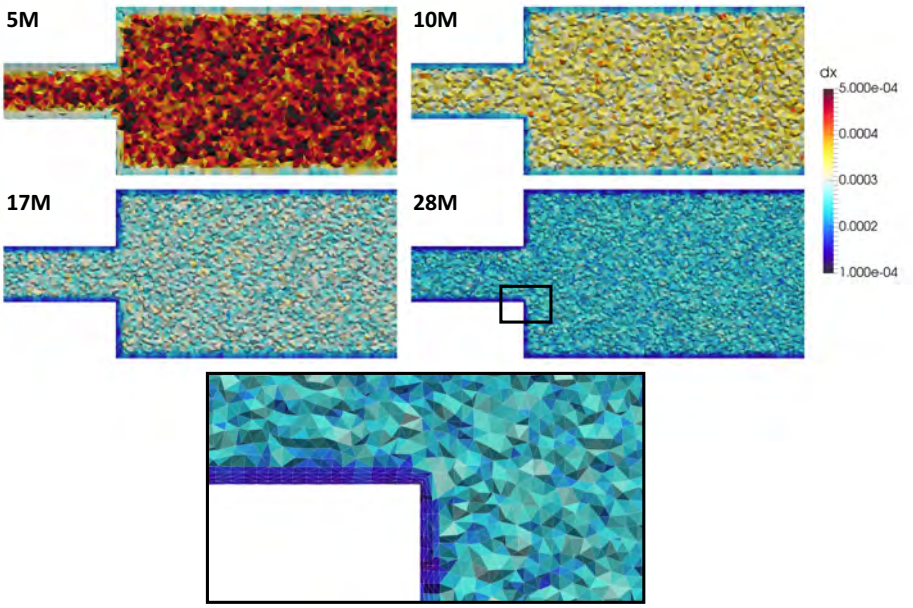

Figure 3.3: The mesh at the sudden expansion. The characteristic length of each cell, dx is computed as Δx in equation (3.10). The lower figure is zoomed in on the finest mesh to see the boundary layer.

explicit time stepping schemes demanded to be < 1. A physical interpretation is that a point in the fluid will not travel further than one cell length in each time step.

The time step is kept fixed under the spatial refinement study, and need to be sufficiently small in order to not influence the solution in comparison with the mesh. An appropriate Δt was found by taking the minimum characteristic cell length in the 28M mesh and the maximum velocity (from previous published results), and then setting that the Courant number should be less than 0.5 for this theoretical worst-case scenario. This resulted in $\Delta t = 1 \cdot 10^{-5}$.

All computations were started with the initial condition that the fluid is at rest. The boundary conditions were set to be $p = 0$ at the outlet, no-slip velocity along the wall and a parabolic profile at the inlet

$$u = 2u_0\Big(1 - \frac{r^2}{r_0^2}\Big) \qquad \text{for } z = -0.12 \tag{3.12}$$

where $r = \sqrt{x^2 + y^2}$. Let A be the area of the inlet (computed for each mesh) and let Q be the flow rate given in Table 3.2 then $u_0 = \frac{Q}{A}$ and

$r_0 = \sqrt{\frac{A}{\pi}}$.

Let the instantaneous velocity (u_i) be expressed as $u_i = \overline{u} + u'$, where $\overline{u}$ is the time averaged velocity and u' is the fluctuating velocity. As both quantities are needed in the analysis, both u and $\overline{u}$ are collected at multiple locations. Statistics are collected using *Probe* and *StatisticsProbe* from fenicstools [59]. A *StatisticsProbe* stores the $\overline{u}$ only and does not include any history from the point. A *Probe*, however, stores the velocity from each time step. Along the centerline, there are 10000 *StatisticsProbes*, and for each slice there are 1000 *StatisticsProbes*. The location of the slices are shown in Figure 3.1. In addition, 540 *Probes* are placed in the geometry, along the centerline and $\pm D/3$ and $\pm 2D/3$. These statistics are equally defined for pressure, except that the pressure is not measured in the slices. The statistics are set to start sampling after 0.4 seconds, following the study of Passerini et al. (2013) [56].

To analyze the statistics from the probes, two indices are computed: turbulent kinetic energy ($k(t)$) and power spectral density of $|u'|$. Turbulent kinetic energy is defined as $k(t) = \frac{1}{2}(u'^2 + v'^2 + w'^2)$. With Fourier transformations, all physical signals can be decomposed into a finite number of frequencies with a corresponding amplitude. From this, the power spectral density can be computed to investigate the amount of 'power' in each frequency. To reduce the level of noise in the power spectral density, Welch's method is applied. The idea of Welch's method is to split the signal into segments, and each segment is then modified by using a windowing function. The next step is to compute the periodogram of each modified segment and then computing the average of all the periodograms [60]. This method reduces the level of noise, but there is a tradeoff as the lowest frequencies will be removed when length of the segments is reduced. Here the signal is split into 8 segments and modified by a Hanning windowing function with 50% overlap. The altered periodogram is computed for each segments, and averaged over all segments.

One of the characteristics of a turbulent flow is the presence of an energy cascade over a wide range of scales. This energy cascade consists of eddies transferring energy from larger eddies to subsequently smaller eddies, and into dissipation (although dissipation happens over a range of scales). Thus, eddies exist over a wide range of sizes or scales. From Kolmogorov (1941), we have that there is limit on the smallest scales that can exist in a flow, referred to as Kolmogorov's scales [61]. The scales are an expression of the real life physics, and not the numerical simulation. The smallest eddies that can be described by the numerical solution are limited by the cell size in the mesh. Consequently, when comparing the Kolmogorov scales to the scales in the numerical simulation, it can indicate how well the temporal and spatial resolution of the numerical problem is. By observing the cumulative dissipation as a function of Kolmogorov length scale we find that if the

characteristic length of a cell is 20 times lager than the smallest Kolmogorov length scale, only ∼45% of the dissipation is resolved. For ten times the Kolmogorov scale it is about ∼85% [33]. These estimates assume a uniform mesh at the location of the turbulent flow. Since the scales only depend on the rate-of-dissipation (ϵ) and kinematic viscosity (ν), the estimate of the Kolmogorov scale might change when the mesh is refined. For instance, refining a mesh may lead to a phenotypically different flow and will change the rate-of-dissipation. In this thesis, two different approaches are used to compute how resolved the mesh is. The first approach is the Kolmogorov scales which are defined as

$$\eta = \left(\frac{\nu^3}{\epsilon}\right)^{\frac{1}{4}} \tag{3.13}$$

$$u_\eta = (\epsilon\nu)^{\frac{1}{4}} \tag{3.14}$$

$$\tau_\eta = \left(\frac{\nu}{\epsilon}\right)^{\frac{1}{2}} \tag{3.15}$$

where η is the length scale, u_η is the velocity scale, and τ_η is the time scale. The rate of dissipation ϵ is defined as $\epsilon = 2\nu < S, S >$, where S is defined $S = \frac{1}{2}(\nabla u + (\nabla u)^T)$, and $< \cdot, \cdot >$ is L^2 an inner-product.

The second approach is a simplified measurement of the Kolmogorov scales from Statistical Theory and Modeling for Turbulent Flows (2001), that indicates the rate between characteristic length of a cell and the Kolmogorov scale for l^+ and the same for the time scale for t^+ [62]. This simplified measurement was introduced in the biomedical flow literature by Valen-Sendstad et al. (2011) [63], and is defined as

$$l^+ = \frac{u_\star \Delta x}{\nu} \tag{3.16}$$

$$t^+ = \frac{u_\star^2 \Delta t}{\nu} \tag{3.17}$$

where $u_\star$ is defined as $u_\star^2 = \nu < S, S >^{1/2}$. It is also noteworthy that t^+ is not correctly defined by Valen-Sendstad et al. (2011), missing Δt [63].

3.2.2 Results

Results of the spatial refinement study are presented in Figure 3.4. There are four different plots in the figure: the instantaneous velocity fields at t = 1.0 s and the velocity, turbulent kinetic energy, and the power spectral

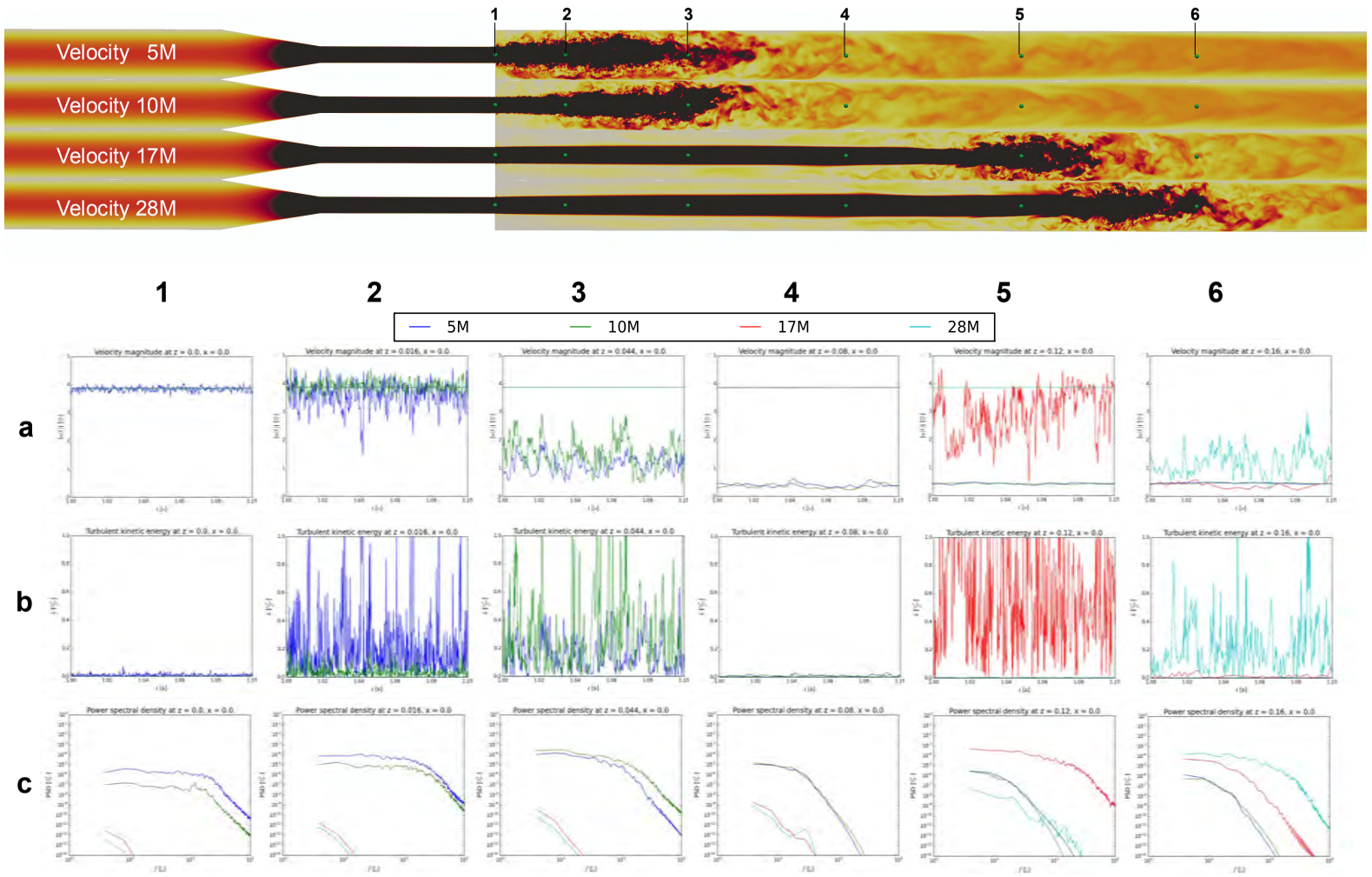

Figure 3.4: The top show instantaneous velocity fields from four of the simulations with Re = 3500 at t = 1.0 s. The plots show **a** velocity traces, **b** turbulent kinetic energy, and **c** the power spectral density of $|u'|$, all from 1.0 to 1.1 s.

density of $|u'|$ is presented at 6 points along the centerline from 1.0 to 1.1 s. Starting at the top, we can first see that the simulations with the 5M and 10M mesh have instabilities in the flow penetrating the sudden expansion. This causes the jet to break down just downstream of the sudden expansion. For the 17M and the 28M simulations, the flow penetrates the sudden expansion unaffected, and subsequently the jet breakdown is delayed. Observing plot **1a** and **1b**, there are already visible fluctuations in the velocity fields for the 5M simulation. However, looking at **1c** we can see that the 10M simulation also harbors fluctuations, although two orders of magnitude smaller. Looking at plot **2a** and **2b**, just downstream of the sudden expansion, the 5M and 10M simulation are clearly unstable, but the velocity at the centerline is still high. In plot **2c**, the energy spectra from the 5M and 10M simulations show that there is a large amount of energy for a wide spectra of low frequent fluctuations. Further downstream, in plot **3a**, we can see that the centerline velocity is reduced and in **3b** that the fluctuations are less high-frequent for 5M and more high-frequent for the 10M simulation. This is reflected in plot **3c** as well, where the low frequent parts of 5M are unchanged, but start to decline earlier. For the 10M case there is a general increase in energy for all frequencies. Further downstream in plot **4a** and **4b** the 5 and 10M simulation are now almost identical, the centerline velocity is almost stabilized and has only small and low frequent fluctuations. In plot **4c**, the 17M and 28M indicate that the instabilities are growing. In addition, the 5 and 10M simulation power density spectra are now smaller as there is no energy at the higher frequencies. Now, 10 diameters downstream of the sudden expansion, the 17M jet breaks down and can be viewed in plot **5a** and **5b**. The energy spectra plot **5c** shows that the 28M simulation also has increased instabilities. In the last column in Figure 3.4, we can see that the centerline velocity of 5M, 10M, and 17M now are of the same magnitude, although 17M have larger fluctuations. The jet in the 28M simulation has at this point started to break down and is clearly shown in plot **6a**, **6b**, and **6c**. The energy spectra of the 17M simulations also starts to lose width and is decreasing.

To supplement the instantaneous values, time averaged quantities are presented in Figure 3.5. The overall agreement with the experimental results for the $Re = 3500$ are poor, as the 17M and 28M simulation break down 10 and 15 diameters downstream of the results from the experiments, respectively. The spatial refinement study did not obtain a monotonically converging solution, i.e., mesh independence. Observing only the 5M and 10M simulations, the results appear to converge towards the experimental results.

Mesh sensitivity was evaluted by the Kolmogorov scales, and the results are presented in Table 3.4. Only the Δx_{mean} is reported since the minimum and maximum value only refers to some special elements in or by the boundary

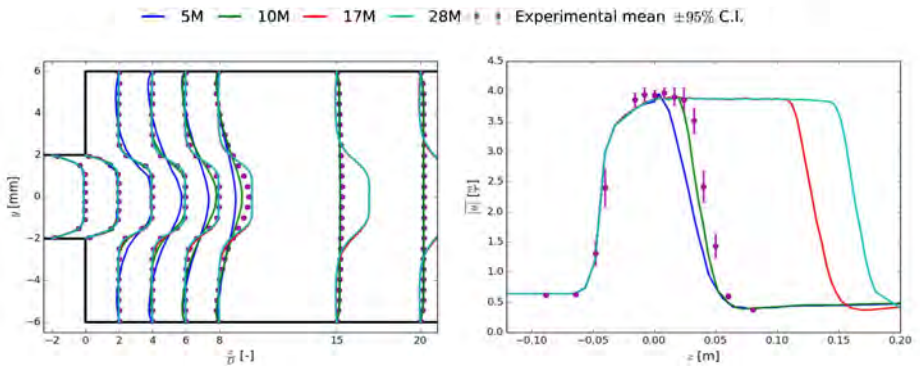

Figure 3.5: Results from the spatial refinement study, statistics collected from 1.4 s to 1.6 s.

layer. Equally, we are only interested in the smallest possible scales in the flow described by η_{min} and l^+_{max}, which are found at the location of the jet breakdown. Since the Kolmogorov scales depend on ϵ for constant ν, they will not be constant since the gradients will change when the mesh is refined. However, remembering that 10M P2-P1 is equivalent to 80M P1-P1, the minimum length scale is converging towards $8.0 \cdot 10^{-6}$. Comparing ratio of Δx_{mean} and η_{min}, we observe that it is substantially larger than l^+. On the other hand, the differences between $\Delta x_{mean}/\eta_{min}$ and l^+ are decreasing from 11.3 for the 5M simulation down to 6.3 for 10M P2-P1. Looking closer at the two estimates for the 10M P2-P1 simulation, the Kolmogorov length scale suggests that the cell size is 17 times larger than the smallest scales, while $l^+ = 11$. These estimates correspond to resolving ∼55% and ∼85% of the dissipation, respectively.

Observing the temporal resolution in Table 3.5, the time step is smaller than the smallest Kolmogorov time scale ($\tau_{\eta,min}$) which means that the simulation is well resolved in time. Furthermore, since the smallest scales is not present in the simulation, the temporal is better than this estimate. The Courant

	5M	10M	17M	28M	10M P2-P1
Δx_{mean}	$3.5 \cdot 10^{-4}$	$2.8 \cdot 10^{-4}$	$2.4 \cdot 10^{-4}$	$2.0 \cdot 10^{-4}$	$1.4 \cdot 10^{-4}$
η_{min}	$9.8 \cdot 10^{-6}$	$9.0 \cdot 10^{-6}$	$8.7 \cdot 10^{-6}$	$8.3 \cdot 10^{-6}$	$8.1 \cdot 10^{-6}$
$l+_{max}$	24.4	19.8	18.2	15.0	11.0
$\frac{\Delta x_{mean}}{\eta_{min}}$	35.7	31.1	27.6	24.1	17.3

Table 3.4: Length scales for each mesh used in the spatial refinement study. The analysis is performed taking the average over 2000 time steps with 20 steps between each and then computing the indices presented in this table. For P2-P1 Δx is divided by 2.

	5M	10M	17M	28M	10M P2-P1
Δt	$1.0 \cdot 10^{-5}$	$1.0 \cdot 10^{-5}$	$1.0 \cdot 10^{-5}$	$1.0 \cdot 10^{-5}$	$5.0 \cdot 10^{-6}$
$\tau_{\eta,min}$	$2.9 \cdot 10^{-5}$	$2.5 \cdot 10^{-5}$	$2.3 \cdot 10^{-5}$	$2.1 \cdot 10^{-5}$	$2.0 \cdot 10^{-5}$
C_{max}	0.17	0.21	0.28	0.3	0.21
$t+_{min}$	1.20	1.10	1.00	0.98	0.97

Table 3.5: Time scales for each mesh used in the spatial refinement study. The analysis is performed taking the average over 2000 time steps with 20 steps between each, and then computing the indexes presented in this table. One exception of this is C_{max} which is the maximum of all time steps.

number is well below the critical limit, and assures that a particle does not travel too far in comparison with the cell length of each time step.

Since the 17M simulation with $Re = 3500$ was the first simulation that has a breakdown further downstream, this mesh will be used for the simulations in the temporal refinement study and the simulations with other Reynolds numbers.

The results of the temporal refinement study is presented in Figure 3.6. The location of the two finest temporal resolved simulations, $\Delta t = 1 \cdot 10^{-5}$ and $5 \cdot 10^{-5}$, is equal. However, the length of the breakdown is shorter in $\Delta t = 1 \cdot 10^{-5}$. This is a general trend, the length of the breakdown increases as the temporal resolution decreases.

Lastly, the results from the other Reynolds numbers are presented in Figure 3.7. The $Re = 500$, 5000, and 6500 simulations are very close or identical to, the experimental data. However, both the transitional simulations $Re = 2000$ and 3500 are phenotypically different from the experimental values and from previous studies. Furthermore, there are some issues with the $Re = 6500$ case as well, in particular the initial jet breakdown. The sharpness of the jet is not properly captured at two diameters downstream from

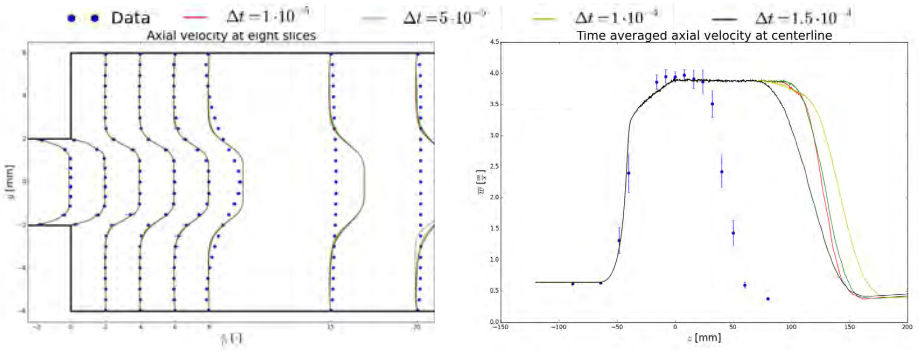

Figure 3.6: Results from the temporal convergence study.

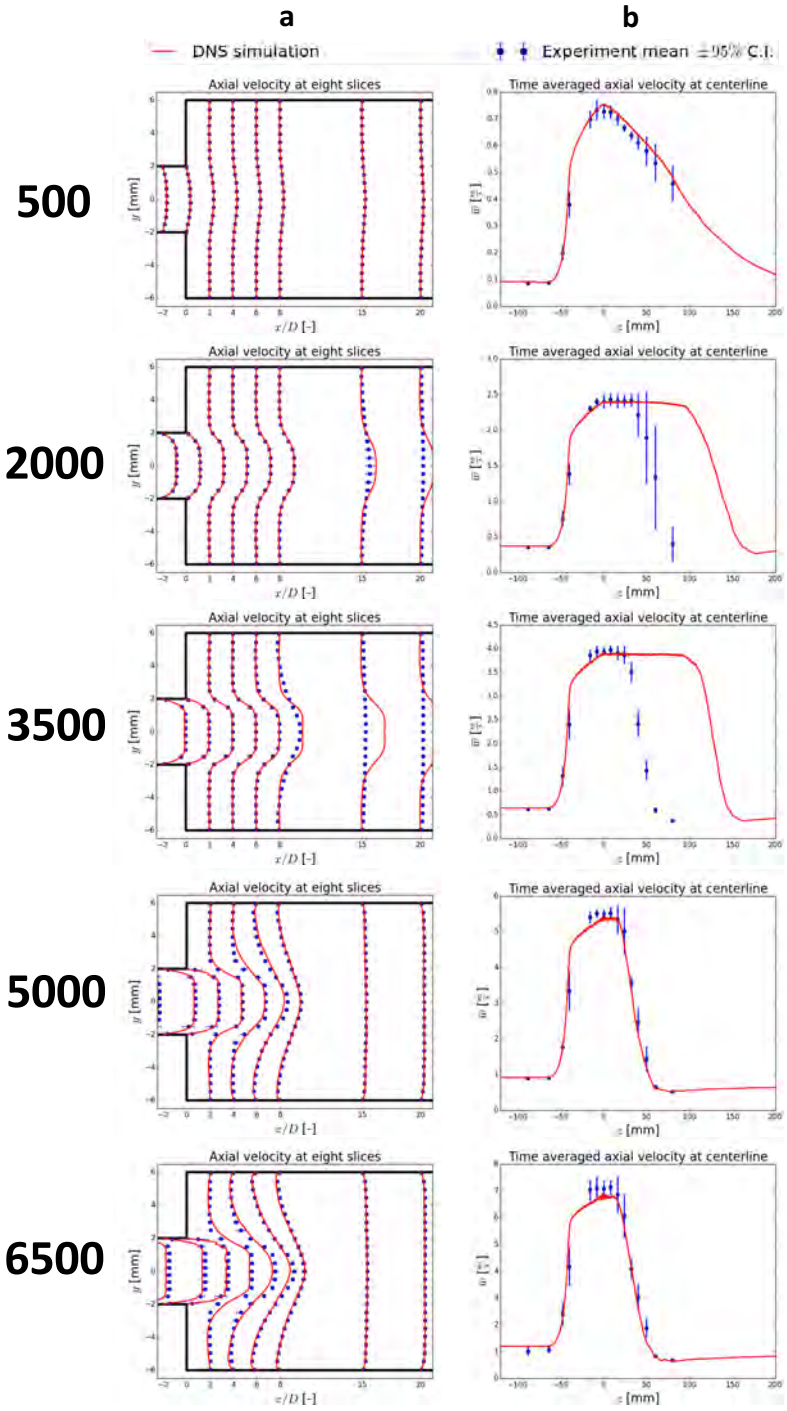

Figure 3.7: Results from each Reynolds number. The $Re = 500$, 5000, 6500 simulations show good agreement, but the transitional cases $Re = 2000$, 3500 have a phenotypical different solution than previously reported.

the sudden expansion. Otherwise the rest of the 6500 simulation has, in comparison with previous studies [54], good agreement with the experimental results.

3.2.3 Discussion

The goal of this study was to validate the solver, but it appears to be falsified instead. Before drawing any conclusions, let's first have a closer look at the problem. First of all, only the $Re = 2000$ and 3500 simulations show discrepancies, and only for the finer meshes. Furthermore, results from other cases are close to perfect. The question is then: Is the jet supposed to trigger to turbulence for the transitional cases? Since the case is two plane symmetric, a starting point for this discussion could be to recast Navier-Stokes equations (2.1) in cylinder coordinates.

$$r : \rho\left(\frac{\partial u_r}{\partial t} + u_r\frac{\partial u_r}{\partial r} + \frac{u_\phi}{r}\frac{\partial u_r}{\partial \phi} + u_z\frac{\partial u_r}{\partial z} - \frac{u_\phi^2}{r}\right) = \tag{3.18}$$
$$-\frac{\partial p}{\partial r} + \mu\left[\frac{1}{r}\frac{\partial}{\partial r}\left(r\frac{\partial u_r}{\partial r}\right) + \frac{1}{r^2}\frac{\partial^2 u_r}{\partial \phi^2} + \frac{\partial^2 u_r}{\partial z^2} - \frac{u_r}{r^2} - \frac{2}{r^2}\frac{\partial u_\phi}{\partial \phi}\right] + \rho g_r$$
$$\phi : \rho\left(\frac{\partial u_\phi}{\partial t} + u_r\frac{\partial u_\phi}{\partial r} + \frac{u_\phi}{r}\frac{\partial u_\phi}{\partial \phi} + u_z\frac{\partial u_\phi}{\partial z} + \frac{u_r u_\phi}{r}\right) = \tag{3.19}$$
$$-\frac{1}{r}\frac{\partial p}{\partial \phi} + \mu\left[\frac{1}{r}\frac{\partial}{\partial r}\left(r\frac{\partial u_\phi}{\partial r}\right) + \frac{1}{r^2}\frac{\partial^2 u_\phi}{\partial \phi^2} + \frac{\partial^2 u_\phi}{\partial z^2} + \frac{2}{r^2}\frac{\partial u_r}{\partial \phi} - \frac{u_\phi}{r^2}\right] + \rho g_\phi$$
$$z : \rho\left(\frac{\partial u_z}{\partial t} + u_r\frac{\partial u_z}{\partial r} + \frac{u_\phi}{r}\frac{\partial u_z}{\partial \phi} + u_z\frac{\partial u_z}{\partial z}\right) = \tag{3.20}$$
$$-\frac{\partial p}{\partial z} + \mu\left[\frac{1}{r}\frac{\partial}{\partial r}\left(r\frac{\partial u_z}{\partial r}\right) + \frac{1}{r^2}\frac{\partial^2 u_z}{\partial \phi^2} + \frac{\partial^2 u_z}{\partial z^2}\right] + \rho g_z.$$

Equation (3.18) - (3.20) can be further simplified. The mathematical problem is independent of ϕ since the geometry, initial condition, boundary condition, and the source function f are independent of ϕ. The equations (3.18)-(3.20) can then be rewritten to

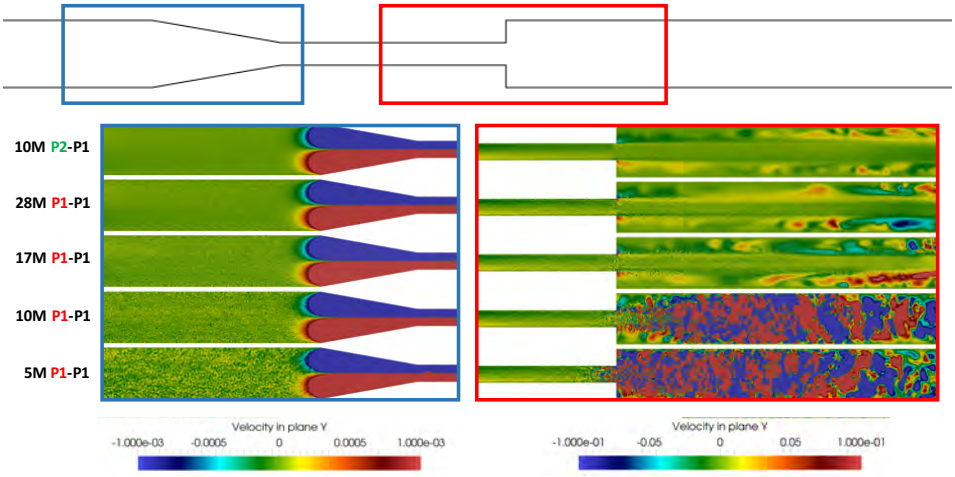

Figure 3.8: Velocity component in y-direction in the y-plane. With a perfect mesh this should be zero before the nozzle. In the blue section (to the left) the noise reduces from the course mesh (5M) to the fine mesh (28M), but from P1-P1 to P2-P1 elements there is a clear reduction in the level of noise. In the red section (to the right) we can observe that the level of noise at the outlet is just low enough in the 17M simulation for the jet not to break down just downstream of the sudden expansion.

$$r : \rho\left(\frac{\partial u_r}{\partial t} + u_r\frac{\partial u_r}{\partial r} + u_z\frac{\partial u_r}{\partial z}\right) = \tag{3.21}$$
$$-\frac{\partial p}{\partial r} + \mu\left[\frac{1}{r}\frac{\partial}{\partial r}\left(r\frac{\partial u_r}{\partial r}\right) + \frac{\partial^2 u_r}{\partial z^2} - \frac{u_r}{r^2}\right] + \rho g_r$$
$$z : \rho\left(\frac{\partial u_z}{\partial t} + u_r\frac{\partial u_z}{\partial r} + u_z\frac{\partial u_z}{\partial z}\right) = \tag{3.22}$$
$$-\frac{\partial p}{\partial z} + \mu\left[\frac{1}{r}\frac{\partial}{\partial r}\left(r\frac{\partial u_z}{\partial r}\right) + \frac{\partial^2 u_z}{\partial z^2}\right] + \rho g_z$$

From equation (3.21)-(3.22) it follows that mathematically this is a 2D problem, which theoretically can not transition to turbulence. However, this is only the mathematical problem. In reality, i.e., in experiments, some level of noise or perturbations are always present, which will break the symmetry, making the flow a 3D problem. The asymmetry can in turn make the flow transition to turbulence. In numerical simulations the mesh will, in finite element method, never be perfect and will always introduce some asymmetry by a finite level of noise or perturbations.

To further investigate the level of the asymmetry, or noise, introduced by

the mesh, we observe the y-component of the velocity in Figure 3.8. From Figure 3.8 it is evident that the magnitude of the fluctuations at the sudden expansion determine where the jet breaks down. Therefore, the next line of investigation is transition to turbulence in channel flow. This has been studied for over 130 years, ever since Reynolds' experiments in 1883 [64]. From the experiments, Reynolds suggested a dimensionless parameter to describe flow in a pipe $Re = \frac{uL}{\nu}$, where u is the velocity, L is the characteristic length and ν is the kinematic viscosity. Depending on Re, the flow is expected to be either laminar, transitional or fully turbulent. The critical Reynolds number for transitional and turbulent regimes are, in modern textbooks and articles, normally reported within the range of 1750-2300 [65, 66, 67], and up to 3000 [68]. However, Reynolds also reported that he observed laminar flow in the range from $Re = 1700$ and up to $Re = 13000$. He suggested that the level of noise introduced by the experiment, or the surroundings, drastically changed the outcome of the experiments [64]. A later experiment for a circular pipe flow has shown laminar flow for Re up to $1 \cdot 10^5$, by taking extreme care not to introduce noise [69]. For a circular pipe flow it is then no longer relevant to look at the critical Re, but rather the critical threshold for noise introduced, before it grows and triggers turbulence.

The effect of noise in transition to turbulence is still an active field of research, and has made significant advances using spectral elements. Hof et al. (2003) found that the critical noise scales with $\frac{1}{Re}$ [70] and, depending on the type of noise, Peixinho et al. (2007) found an even stronger scaling [71]. Furthermore, these results of scaling are consistent with other numerical and experimental studies [72, 73, 74, 68, 65]. Mullin (2005) showed that $Re \lesssim 1750$ is not sensitive to perturbations, and can be considered as a lower limit for the scaling law found by Hof et al. (2003) [75]. Collecting the evidence from the literature, we have the following scaling law for flow in a pipe

$$Threshold \sim (Re - \beta)^{\alpha} \qquad \text{for } Re > \beta \tag{3.23}$$

where Re is the Reynolds number, α is a constant in the interval $[-1.5, -1]$ depending on the type of noise introduced, and β is a constant around 1750. This theory is consistent with the results reported in the refinement study, since a finer mesh will introduce smaller perturbations and eventually become lower than some critical threshold. Furthermore, it is also consistent with the results for the $Re = 500$, $Re = 5000$, and $Re = 6500$ simulations since the scaling law is not valid for $Re = 500$ and $Re = 5000$ and $Re = 6500$ would need very fine meshes to come below the critical threshold. For the $Re = 2000$ simulation, the results are also as expected. The scaling law provides a plausible explanation for all the results produced in the study.

If the scaling law is correct, the $Re = 2000$ case should not be sensitive to noise. Consequently, it should be easy to obtain a phenotypically different flow compared to the experimental results. In Figure 3.7, we can observe that the $Re = 2000$ case has an abnormally large confidence interval on the measurement in the middle of the jet breakdown. This stems from a variation in one of the experiments where they applied a large tank instead of a small tank [57]. To test the sensitivity, a simulation using the 10M mesh for the $Re = 2000$ was performed. The simulation diverged when the jet propagated through the entire domain and caused backflow at the outlet. This result backs up the sensitivity observed in the experiments and is consistent with the scaling law (3.23).

To further investigate the plausibility of the numerical results, noise was added at the inlet to mimic the experimental setup. As indicated by the $Re = 2000$ case, experiments are never perfect, and some finite level of noise is always introduced in form of one or more of the following: minor pulsations in the flow rate due to the pump, sound in the room, transition between pipes, irregular surface in the geometry, non-symmetric geometry, or similar. Here we assumed that the flow straightener in the experiment is not perfect and that some noise in the angular direction is present. Furthermore, some noise is also added to the parabolic inlet profile, and is implemented by

```
class InnExpression(Expression):
    def eval(self, value, x):
        r = np.random.uniform(0.99, 1.01)
        value[0] = u_0 * (1 - (x[0]*x[0] + x[1]*x[1])\
                                    / (r_0*r_0)) * r

class Noise(Expression):
    def eval(self, value):
        value[0] = np.random.normal(0, 1e-3)
```

Listing 1: Boundary condition to add noise at the inlet. u_0, and r_0 is as defined in equation (3.12)

Using the new inlet conditions with noise in the angular direction and the 17M mesh the $Re = 500$, $Re = 3500$ and $Re = 6500$ cases were simulated again with the same Δt as previous. The results are presented in Figure 3.9. Both the results in $Re = 500$ and $Re = 6500$ are unaffected, for $Re = 500$ the error is of magnitude $\mathcal{O}(10^{-7})$. The normal simulation (blue) and the simulation with noise (green) are indistinguishing in Figure 3.9 for the $Re = 500$ and 6500. In contrast, the $Re = 3500$ simulation gives a phenotypically different result, which is similar to the experimental results. Thus, the transitional solution is much more sensitive to the artificial noise. The results are in accordance with the theory presented above. Admittedly,

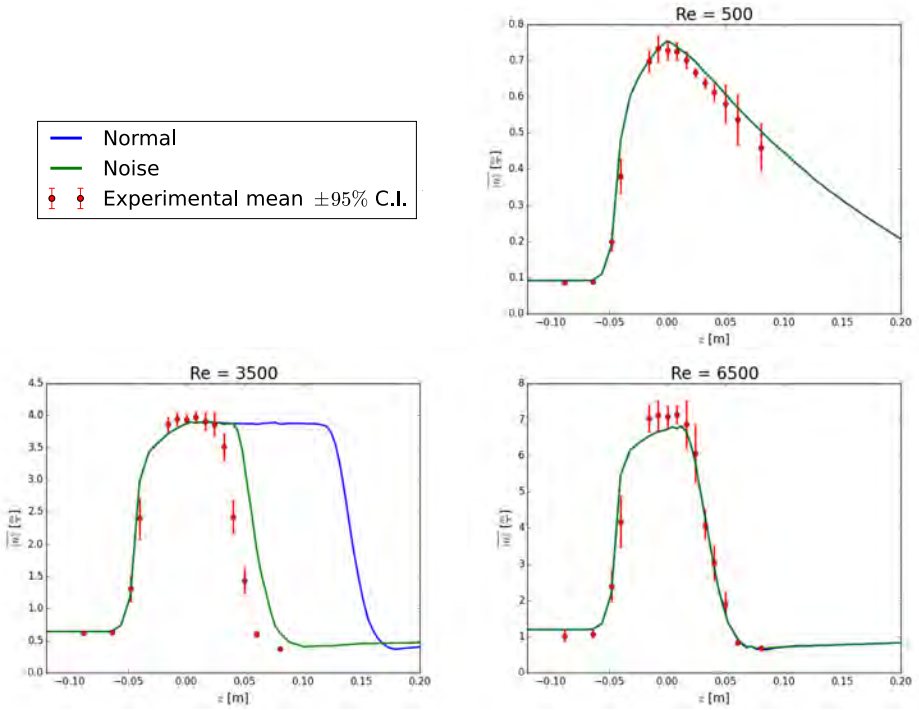

Figure 3.9: The effect of adding noise at the inlet. In the $Re = 500$ simulation there is no difference between the two simulations, for $Re = 3500$ the breakdown of the jet becomes phenotypical similar to the experimental values, and for $Re = 6500$ there is almost no difference between the normal simulations and the one with noise.

the $Re = 3500$ does not show a perfect agreement with the experimental results, but this is only intended as a proof of concept that noise could phenotypically change the transitional simulations.

The results are in agreement with the theory presented in the literature, but are they consistent with previous studies? In the original challenge, 28 groups submitted results, all using Reynolds-Averaged Navier-Stokes (RANS) with zero-, one- or two-equation models. This is arguably not state-of-the-art CFD [33]. In light of the results from the original study, four non-blind studies were performed using direct numerical simulation (DNS) [56], large eddy simulation (LES) [54, 55] and a dynamic hybrid RANS/LES model [53]. All the retrospective studies showed reasonable agreement with the experimental results. However, only Passerini et al. (2013) and Delorme et al. (2013) performed a spatial refinement study, for the $Re = 500$ and $Re = 2000$ case, respectively [56, 55]. The studies from Passerini et al. (2013) and Delorme et al. (2013) were also the only studies that obtained agreement with the experimental results for the $Re = 3500$

case. These will therefore be used for comparison.

We start by comparing the results presented here with the results from Passerini et al. (2013). The meshing approach is different, as they report that they found *"(...) a sufficient level of refinement for the different regions of the domain"*, compared to the uniform approach in this study. The mesh used in the study has ∼3M cells with P2-P1 elements and reports $l^+_{max} = 4$, which is significantly better than the 10M P2-P1 simulation with $l^+_{max} = 11$ in this thesis. Since the mesh is well resolved at the location of the breakdown, it is likely that the mesh is coarser in the nozzle and further upstream. The coarser part might have introduced asymmetry in the flow that caused the jet to break down in accordance with the experimental results. These are just speculations, and should be justified by reproducing the results. However, there is not enough information in the study to reproduce the mesh [56]. Furthermore, they use a time step $\Delta t = 1.0 \cdot 10^{-4}$ which is substantially larger than other retrospective studies [54]. Lastly, a substantial difference is the choice of discretization, as they used a coupled approach instead of a fractional step method as applied in *Oasis*. How this affected the solution has not been tested. The comparison has no concrete evidence to either backup or falsify the results presented in this thesis. The level of refinement in the mesh provides a plausible explanation of why the results are phenotypically different.

For the study from Delorme et al. (2013), it is harder to compare the results as they use finite volume method and LES instead of finite element method and DNS approach. However, they performed a refinement study on the $Re = 2000$ case, where the finest mesh had $96 \times 96 \times 768$ unknowns, which is equivalent to a ∼40M P1-P1 mesh with tetrahedrons. Despite a mesh with such high resolution, the reported results are in perfect agreement with the experimental results. Looking at the vorticity reported for the $Re = 2000$ case, the flow is already turbulent or highly unstable in the sudden expansion. To investigate the reason for this is beyond the scope of this thesis, as this was only intended as a validation case. However, a quote from the famous mathematician and statistician George P. E. Box might give some insight: *"All models are wrong, but some are useful"* [76]. Assuming the results presented in this thesis to be correct, the model applied by Delorme et al. (2013) seems to be useful as they introduce the same level of noise as the experiment.

For the sake of argument, let's assume that the results from this thesis in fact are correct. This leads back to the original goal of the FDA benchmark quoted in the introduction: *"(..) to assess the current state of the art in CFD modeling with respect to predicting fluid dynamics in an idealized medical device model"*. When doing the computations "correctly", the numerical results are then supposed to be different from the experimental, i.e. "cor-

rect" CFD will give a laminar result for all cases when properly resolved. The experiment could have avoided this problem by not using a two-plane symmetric geometry. Steinman et al. (2003) showed that the experimental results of symmetrical cases were extremely sensitive to small changes [77]. Furthermore, in Varghese et al. (2007), a numerical study of a stenosis, an asymmetric geometry was chosen in order to avoid that the noise would dominate the results [78, 79]. Samuelsson et al. (2015) used DNS results and linear stability analysis to show that an offset of eccentricity by 0.3% of the diameter reduces the critical Reynolds number by 50% in a stenosis [80]. Hence, the stenosis and, by extension, the geometry studied here, are highly sensitive to an offset of eccentricity. The introduction of eccentricity would have created a narrower range of Reynolds numbers that are sensitive to noise, since it would be the asymmetry of the geometry that causes the flow to trigger to turbulence, and not noise from the experiment.

The 28M simulation for $Re = 3500$ never converged as the breakdown of the jet changed in time. The breakdown of the jet propagated though the entire domain and diverged when causing backflow at the outlet. In an attempt to fix this, the last two diameters of the domain were altered to be a nozzle. By adding the nozzle, the 28M simulation ran longer, but eventually it also caused backflow at the outlet. The same modification was also made to the 17M simulation with $Re = 3500$, but this did not change the location of the breakdown. It is likely that the 28M simulation would break down at some point if the computational domain was extended. The problem of the simulation diverging was also encountered in $Re = 2000$ for the 10M and 17M simulation.

The temporal refinement does not impact the solution as much as the spatial refinement study, but the length of the breakdown varies. The two finest simulations, the $\Delta t = 1 \cdot 10^{-5}$ and $\Delta t = 5 \cdot 10^{-5}$, do not differ much. When comparing these against the two others ($\Delta t = 1 \cdot 10^{-4}$, $1.5 \cdot 10^{-4}$), the breakdown is stretched over a longer area and starts earlier. This is as expected since less of the dissipation is resolved. The $\Delta t = 1.5 \cdot 10^{-4}$ is on the very limit of what the solver can handle as $\Delta t = 2 \cdot 10^{-4}$ and higher diverged.

3.2.4 Conclusions

The benchmark has been simulated by over 30 scientific groups from all over the world and none has yet reported the same results as presented here. This leaves the author of this thesis with the burden of proof. However, by adding $1 \cdot 10^{-3}$ noise in the angular direction to the inlet, we can explain the observed discrepancies between the numerical results and those from the experiments. We therefore conclude that the results presented are correct.

Future efforts will be made to gain additional insight into this case by using a spectral element solver and linear stability analysis. In addition, a better understanding of how different types of noise impact the solution will be investigated.

This can potentially explain the discrepancies observed between CFD and experiments in certain cases [81]. In addition, it might also be a contribution to the dangers of choosing a double axi-symmetric case for experiments. The quote from Walter J. Savitch sums it up nicely: *"In theory, there is no difference between theory and practice. But, in practice, there is"* [82].

In the context of *validation*, the solver is now considered validated against the FDA benchmark. Future studies should focus on investigating the point of transition in biomedical flows to further validate the solver.

Chapter 4

An Objective Approach for Manipulating Morphological Features in Arteries

The main goal of this study is to develop an objective approach for manipulating morphological parameters in arteries. In Chapter 1 *Introduction and Medical Background*, four morphological features were mentioned, of these the first two will be addressed: angles in the bifurcation and area variations.

One study by Ingebrigtsen et al. (2004) show that wider angles ($\phi_1 + \phi_2$ in Figure 4.1A) in the bifurcation is statistically correlated with the presence of aneurysms, giving rise to the idea of rotating daughter branches [25]. From this point on, the artery associated with r_0 in Figure 4.1A is referred to as parent artery. r_1 and r_2 are referred to as daughter branches.

The motivation for looking at area variations is the study from Schimansky et al. (2013) that found area variations to be statistically correlated with the presence of aneurysms. Using 2D angiogram images, Schimansky et al. (2013) investigated the ratio between a distal extradural diameter and the largest diameter in the siphon [27], see Figure 4.1B. The distal extradural diameter can not be measured in the models available, as that part of the vasculature is not included in the models. Furthermore, in 2D the diameter is a surrogate parameter for the area, and since we have 3D images, the area will be calculated, instead of the diameter. This motivates the parameter

$$R = \frac{A_{max}}{A_{min}} \tag{4.1}$$

and thus replacing the diameter with the area and distal extradural area

with the minimum area. The goal is therefore to vary R.

To the author's best of knowledge, there is no objective method for changing the morphological features presented in the literature. Therefore, a method for objectively rotating branches and changing the area variation will be presented in this thesis. In the method section, quite a few details are left out, as we strive to present just the bare minimum, enough for the presented method to be reproducible.

The scripts are structured as a framework, making it easy to expand with new methods for manipulation, e.g., manipulate curvature and torsion. Furthermore, the scripts also store statistical parameters describing the morphology which are easy to collect and analyze if needed. The framework can be used for the entire cardiac vasculature system, but is only validated for intracranial arteries.

Another aspect taken into consideration is the possibility to investigate morphological parameters in large scale studies. A problem for large scale studies have been the amount of work performed by the user. Therefore, an additional goal is to minimize the user interaction.

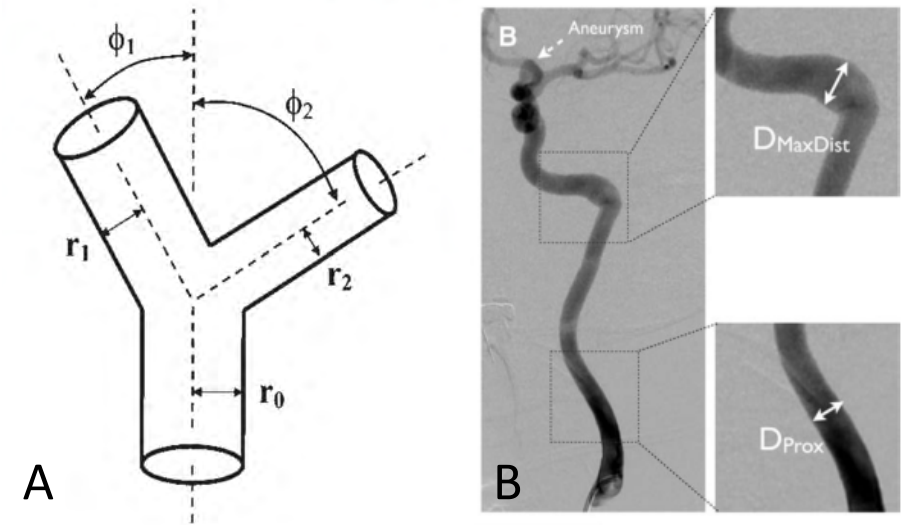

Figure 4.1: **A** shows a schematic view of a bifurcation, where the subscripts 0, 1, and 2 corresponds to the parent artery, smallest daughter branch, and largest daughter, respectively. The figure is taken from Ingebrigtsen et al. (2004) [25]. **B** shows how Schimansky et al. (2013) measured the area ratio [27].

4.1 Method

The framework, named *vmtktools*, is written in Python utilizing *vmtk* [83] and *vtk* [84]. In total, *vmtktools* consists of ∼4000 lines of code, and can be downloaded from *GitHub* at *https://github.com/aslakbergersen/vmtktools*. It includes functionality for pre-processing, extracting statistics, modifying morphology, and post-processing. However, only pre-processing and modifying morphology will be presented here.

The geometric manipulation of the morphology are all built upon the Voronoi diagram [85, 86] and the centerline [87], see Figure 4.2. A Voronoi diagram is an alternative representation of a surface, using spheres. Since a sphere can be uniquely described by a center and a radius, and there is no connectivity between each sphere, the Voronoi diagram is easier to manipulate than a surface or mesh.

4.1.1 Data Acquisition

Ten healthy cases were taken from the ANEURISK project [88]. The images are from 3D rotational angiography for a routine assessment of a cerebral aneurysm at Neuroradiology Division of the Niguarda Ca'Granda Hospital in Milan, Italy. The imaging was performed with an Integris Allura Unit (Philips, Best, the Netherlands), set to the following parameters: C-arm rotation speed, 55 per second; matrix size, 512 9 512; frame rate, 25 frames per second; 18 mL nonionic hydrosoluble contrast agent was injected prior to the acquisition at 4 mL/s [89].

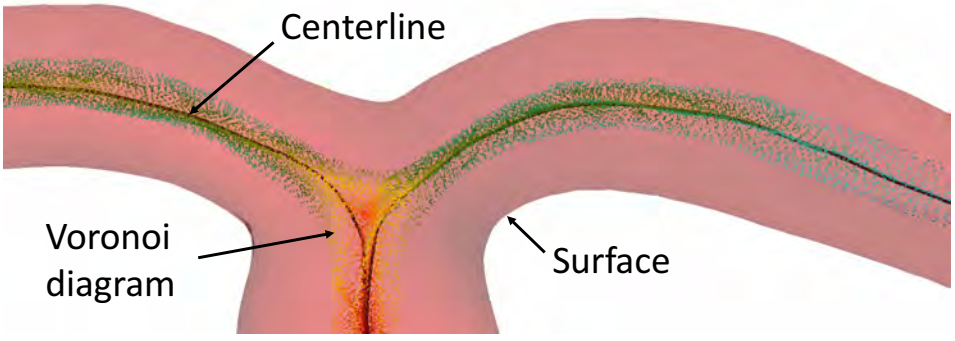

Figure 4.2: An example of a Voronoi diagram representation of a surface, and a centerline.

4.1.2 Pre-processing

To perform a quick pre-processing with minimal user interaction the script *initialize_cases.py* can be executed. It loops over all the cases in a given directory, and the user provides the location of the inlet, outlet, and aneurysm(s) for each case in a particular order. The location is provided through a new method in *vmtk* and is found under *pointselector* in [90]. After providing the input, centerlines and Voronoi diagrams are computed. In comparison to previous published tools [91], this is a ∼30 times speed-up of the process, and is in addition more accurate. This allows for the user to spend ∼2 hours, rather than ∼60 hours, to analyze 100 cases.

4.1.3 Objective Rotation of Daughter Branches

It is simple to just rotate the daughter branches. The main problem is how to objectivly alter the bifurcation when the branches are rotated. The same problem occurs for aneurysm removal in the bifurcation, as the surface prior to disease is unknown. A method to solve this problem is presented in Ford et al. (2009), where the idea is to remove the entire bifurcation, with the aneurysm, and then rebuild it [91]. If the bifurcation was removed and the daughter branches no longer were connected to the parent artery, the daughter branches would be free to rotate without any concern for the bifurcation. This reduces the problem to objectivly reconstructing of the bifurcation after rotation of the daughter branches.

In the study by Ford et al. (2009) they stated: "*Although the current technique successfully removes the aneurysm and reconstructs the parent artery, it has several limitations. (...) As a result, users must exercise their judgment if a particular case is a good candidate for similar studies (. . .)*", before concluding "*(...) the physiological faithfulness of these retrospective reconstructions remains to be verified*" [91]. The latter is difficult because the needed contrast-based high quality medical images cannot be obtained from healthy individuals, and the presence of an aneurysm might affect the morphology of the vasculature. However, having access to angiograms from patients that underwent neurointensive care where no abnormalities were found, a validation test is now possible. Applying the method on 10 cases revealed discrepancies in the apex. From this we hypothesised that an incremental improvement could be made to the original method presented by of Ford et al. (2009).

To fix the discrepancies in the apex, and to obtain a more realistic surface, an incremental improvement of the method from Ford et al. (2009) is presented in Figure 4.3, through steps one to nine. The first four steps are identical to the method in Ford et al. (2009). *Step 1:* Compute the Voronoi diagram

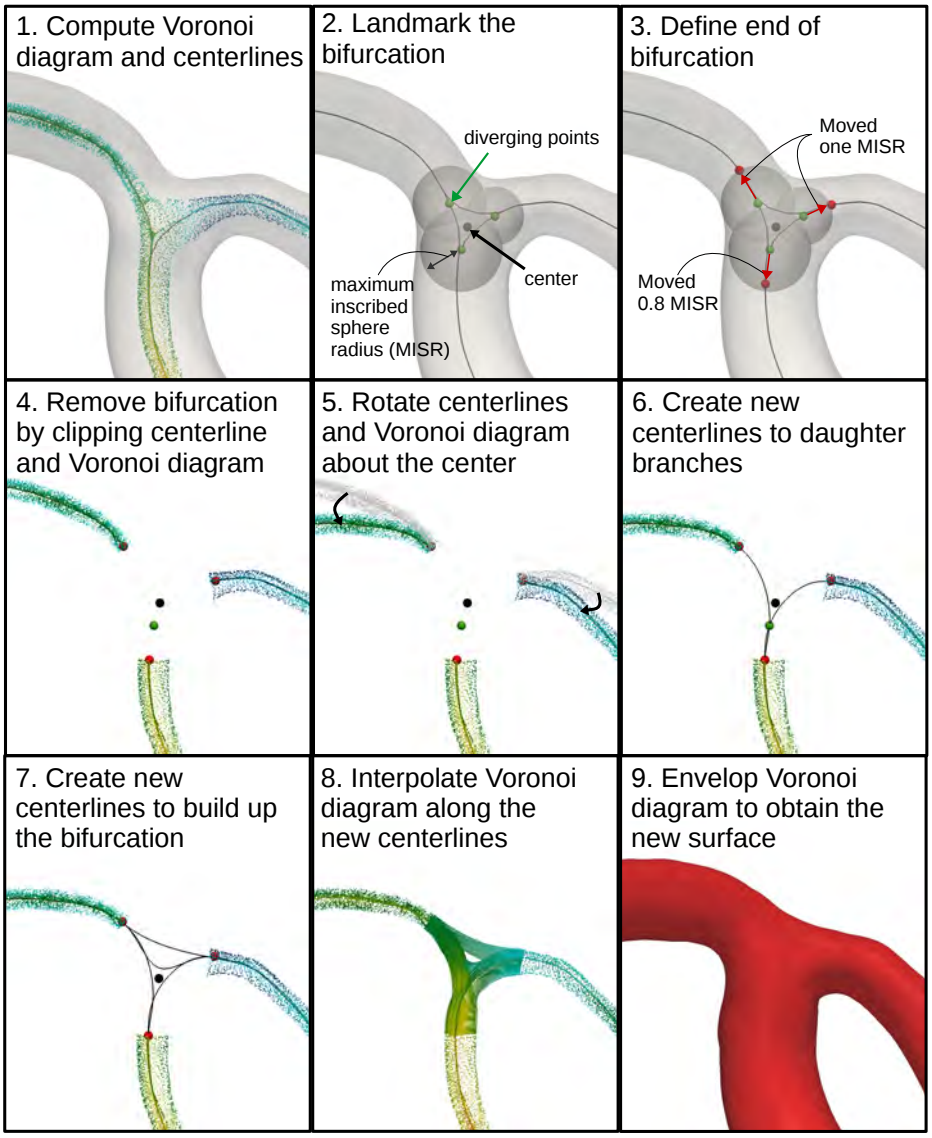

Figure 4.3: Algorithm for rotating daughter branches. In *step 5*, one could choose to only rotate one of the branches, or rotate them the other direction. *Step 7* could be skipped or only include the lower centerline. The lower centerline is forced though the point $c_w = \frac{4}{9}d_1 + \frac{4}{9}d_2 + \frac{1}{9}d_p$, where d is the diverging points (green), and 1, 2, p denotes the largest daughter branch, smallest daughter branch and the parent artery, respectively. This could also be chosen to be the center instead.

and centerlines. This is performed by the pre-processing script. *Step 2:* Landmark the bifurcation by finding the diverging points, the maximum inscribed spheres, and the bifurcation center. This is done by first finding the divergence point, which is where the centerlines are diverging (green points), and the corresponding maximum inscribed sphere (gray). The center is defined as the spatial average of the diverging points. *Step 3:* Find the end of the bifurcation, which is defined as the diverging points moved a distance equivalent to one maximum inscribed sphere radius along the centerline for the daughter branches, and 0.8 for the parent artery. *Step 4:* Remove the bifurcation based on the end points found in step 3. *Step 5*: Rotating the daughter branches is skipped and will be addressed later. *Step 6:* Interpolate new centerlines from the parent artery to both daughter branches, forced through the divergence point of the parent artery. *Step 7:* Interpolate two centerlines between the daughter branches, where the lower centerline is forced though a weighted center $c_w = \frac{4}{9}d_1 + \frac{4}{9}d_2 + \frac{1}{9}d_p$. The subscripts 1, 2, p correspond to the largest daughter branch, the smallest daughter branch and the parent artery, respectively. The lower centerline is present to fix a potential dint in the bifurcation, and is therefore forced though the weighted center, not the center. *Step 8:* Interpolate the Voronoi diagram along the new centerlines using the parallel transport frame [92]. If the Voronoi diagram along the lower centerline affects the surface in the daughter branches, these parts are removed. *Step 9:* Envelop the Voronoi diagram and create a new surface.

Since the code used in Ford et al. (2009) is open source, a substantial part of this was reused. However, only the core algorithm of interpolation for the Voronoi diagram is left unchanged. By replacing specific methods with more general ones, the amount of code was reduced with more than 50%. In addition, some speed-ups were added. For example, in one of the methods, instead of looping over each point in the Voronoi diagram about 1000 times, this was changed to two, making the method more efficient.

Prior to introducing *Step 5*, rotation of the branches, the angles in the bifurcation have to be defined. The most natural approach would be to follow Ingebrigtsen et al. (2004), but the angles were measured manually in that experiment, and the same "rules" translate poorly to an automatized and objective method. However, several methods for measuring the angles are described in the bifurcation in the literature [87, 30, 93]. The approach in these methods is the same: define three vectors representing each branch, and compute the angle by using

$$\varphi_1 = \arccos\left(\frac{v_1 \cdot v_p}{|v_1||v_p|}\right) \tag{4.2}$$

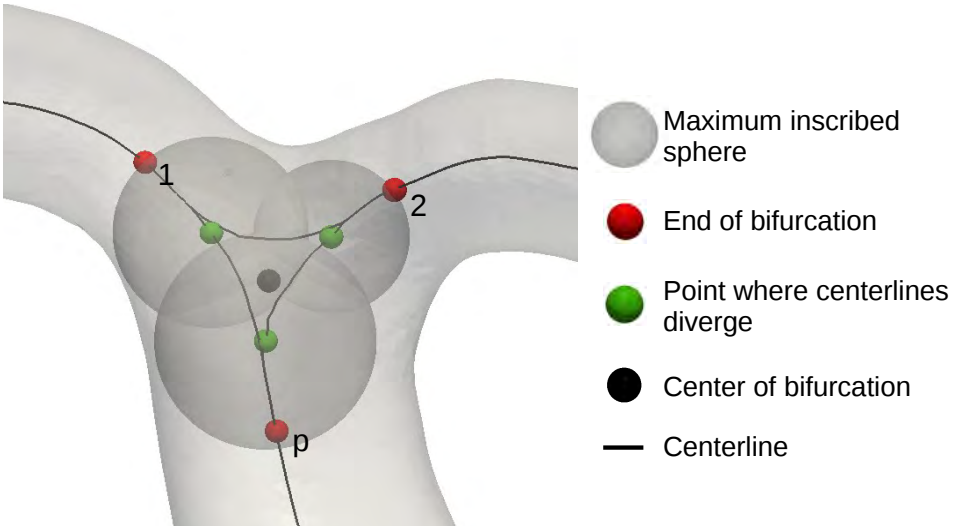

Figure 4.4: Schematic view of a bifurcation. The subscripts 1, 2, and p are for the largest daughter branch, smallest daughter branch, and parent artery, respectively.

where φ_1 is the angle between the largest daughter branch and the parent artery, and v_1 and v_p are vectors for the largest daughter branch and parent artery, respectively. The difference between the methods is how the start and end point of the vectors are defined. Observing Figure 4.4, a more detailed view of a bifurcation, the potential vector from the diverging points (green points) to the end points (red points) gives a good indication of the direction of each branch. This is consistent with the choice made in the study by Picinelli et al. (2012) [89], and is chosen in this thesis as well. In the study from Picinelli et al. (2012) [89] they project the vectors down to the bifurcation plane, defined by the Frenet–Serret frame at the diverging point d_p. Doing so will remove the effect of the branches being out of plane. Although this effect is normally very small (1-2 degrees) in the internal carotid artery terminus, it might be larger in other bifurcations. Therefore, the vectors are chosen not to be projected into the bifurcation plane.

Addressing *Step 5* in Figure 4.3, rotating the daughter branches. In order to preserve the angle with the rest of the vasculature the branches are rotated in the bifurcation plane, spanned by v_1 and v_2, see Figure 4.4. The vectors v_1 and v_2 are expanded to a three dimensional orthogonal base using the Gram-Schmith process. The original coordinate system is first translated to have the center of the bifurcation as origin, and then the system is rotated to have the vectors spanning the new base as unit vectors. The branches are then moved in the bifurcation plane using a standard rotational matrix:

$$R = \begin{pmatrix} \cos\theta & -\sin\theta & 0 \\ \sin\theta & \cos\theta & 0 \\ 0 & 0 & 1 \end{pmatrix} \tag{4.3}$$

By looping through each point in the Voronoi diagram and it identifies which branch the point belongs to. Then based on which branch the point belongs to, the point is rotated θ or $-\theta$. The centerlines are also rotated, and one does not need to compute new centerlines after rotating the daughter branches. The geometries presented in Figure 4.5 and Figure 4.6 is computed executing the following command:

```
pyhton move_branches.py --case [case_name] --lower True --addPoint True
↪  --bif True --angle X
```

The script has multiple options that makes it possible to run either the algorithm presented here, the one presented by Ford et al. (2009), or something in between. For a complete list of options and a longer explanation,run:

```
python move_branches.py -h
```

The method of parent artery reconstruction were originally applied to removing aneurysms. Since the algorithm for doing so is slightly different, this can be performed by a separate script *remove_aneurysm.py*. The script is not applied in this thesis.

4.1.4 Area Variation

The main idea of this method is: Loop over all Voronoi points, move the point relative to the centerline and change the corresponding radius, a factor H_i. The factor H_i has to depend on the area at that point. From the altered Voronoi diagram, one can obtain a new surface. This process can be separated into three steps: *First* step is to obtain the area along the centerline, *second*, compute the factor H_i, and *third*, manipulate the Voronoi diagram.

The *first step* is to compute the area as a function of the length of the centerline s. This is done by using the *makeCenterlineSections* from *vmtk*. However, this module requires that the centerline is sufficiently smooth, if not the method fails. Using the module *centerlinesmoothing* will move the centerline in space when smoothing, and is not robust enough for this

application as there is no guarantee that the centerline is in the middle of the geometry, which is important when moving Voronoi points in step three. One solution is to approximate the centerline using splines, and is implemented using *scipy.interpolate.splrep*. The spline is later converted back to a vtkLine object as the rest of the centerlines.

The *second step* is to create a discrete function H_i used to manipulate the Voronoi diagram. The area should be altered to be either closer to the mean, or further apart, depending on whether R should be increased or decreased. Therefore a factor F_i is suggested

$$F_i = \left(\frac{A_i}{A_{mean}}\right)^{\beta} \tag{4.4}$$

where A_i is the area at point i along the centerline, and A_{mean} is the mean area of the centerline of interest. β is the factor that decides how the area will change. For $-1 \leq \beta < 0$ the ratio R will decrease, for $\beta > 0$ the ratio R will increase, and for $\beta = 0$ there will be no change. In order to ensure that the model can be compared to the original surface, the inlet area has to be left unchanged, but downstream gradually transition over to the new model. The same applies at the end of the area of interest, since the transition between the altered model and the original has to be smooth. This is solved by letting the first and last 10% of the area of interest be a linear combination of the new and old model. Let H_i be the factor moving each point, and $i = 0, \ldots, N$, $m = 0.1N$, $n = 0.9N$, where N is the number of points along the centerline. Then H_i is defined

$$T_i = \begin{cases} \frac{m-i}{m} & i < m \\ 0 & m \leq i \leq n \\ \frac{i-n}{n} & n < i < N \end{cases} \tag{4.5}$$

$$H_i = F_i(1 - T_i) + T_i \tag{4.6}$$

The *third step* is the algorithm for moving the points, as is shown in Algorithm 2. First, loop over all the Voronoi points and check if the point is inside the area of interest. If the point is inside the area of interest, then find the closest point on the centerline and create a vector from the centerline to the Voronoi point. Using this vector and H_i, the new location is computed and the new radius is set to be $r_i^{new} = r_i H_i$. If the point is outside the area

of interest, then it stays unchanged.

Algorithm 2: The algorithm for changing the area of an artery.

for $p_i \in$ *voronoi points* **do**
  if *Inside area of interest* **then**
    c_i = GetClosestPoint(centerline, p_i);
    $v_i = c_i - p_i$;
    $p_i^{new} = p_i + v_i(1 - H_i)$;
    $r_i^{new} = r_i H_i$;
  else
    $p_i^{new} = p_i$;
    $r_i^{new} = r_i$;
  voronoi.addPoint(p_i^{new}, r_i^{new})

Since it is the min/max ratio (R) that we in this case would like to control, the matching β could be found by

$$\begin{aligned} R_{new} &= \frac{A_{max,new}}{A_{min,new}} \\ &= \frac{\pi \left(r_{max} H_{max}\right)^2}{\pi \left(r_{min} H_{min}\right)^2} \\ &= \frac{A_{max} \left(\frac{A_{max}}{A_{mean}}\right)^{2\beta}}{A_{min} \left(\frac{A_{min}}{A_{mean}}\right)^{2\beta}} \\ &= R^{2\beta+1} \\ \beta &= \frac{1}{2}\left[\frac{\ln\left(R_{new}\right)}{\ln\left(R\right)} - 1\right] \end{aligned} \tag{4.7}$$

This does not take into account that H is a linear combination of the new and old model in the beginning and ending of the area of interest. Therefore we have equation (4.7) as an estimate for β to obtain a surface with the desired R_{new}.

The program can be executed by running the following code

```
pyhton area_variations.py --case [case_name] --smooth True --ratio X
```

For a complete list of options and a detailed explanation run

```
python move_branches.py -h
```

The script also has a statistical 'mode' *–stats True*, which computes all of the parameters defined above. There is also a flag for setting stopping point, e.g. ophthalmic, or at bifurcation of interest.

4.2 Results

4.2.1 Objective Reconstruction of Parent Artery

To compare the method for parent artery reconstruction from Ford et al. (2009) [91] and the method presented here, they were both applied to ten geometries from healthy patients. The results are presented in Figure 4.5,

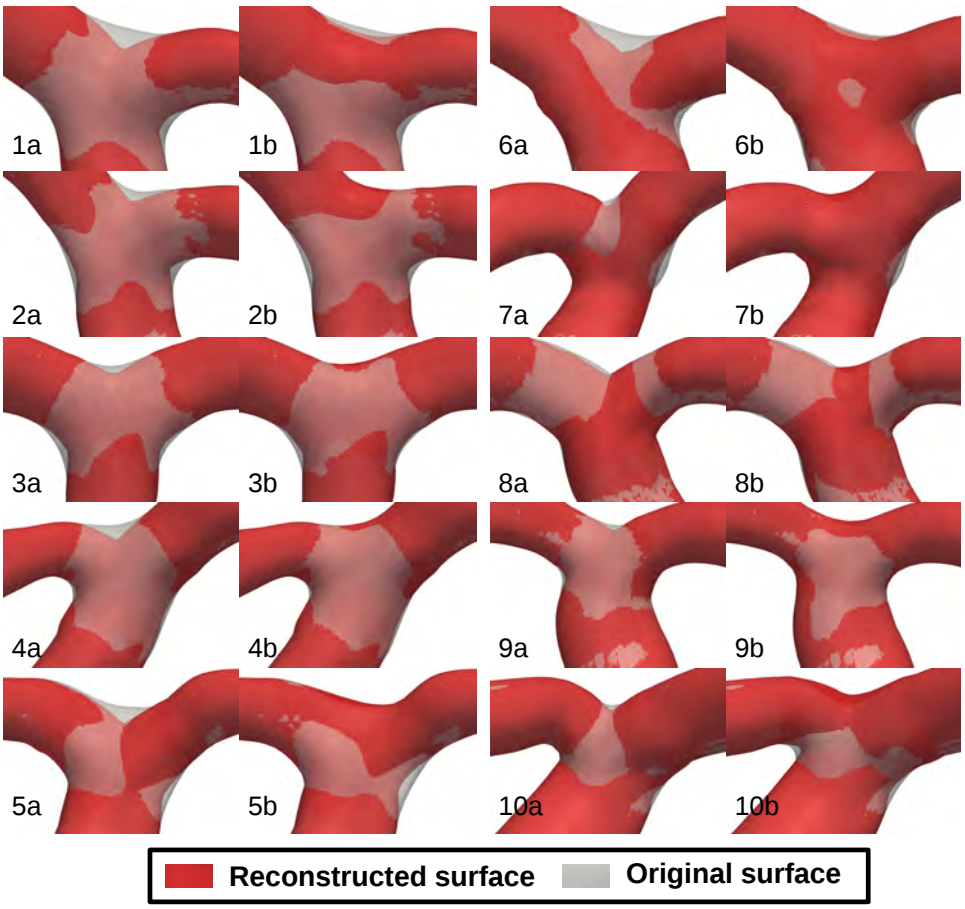

Figure 4.5: A comparison of the method presented in Ford et al. (2009) [91] and the incremental improvement for parent artery reconstruction suggested in this thesis.

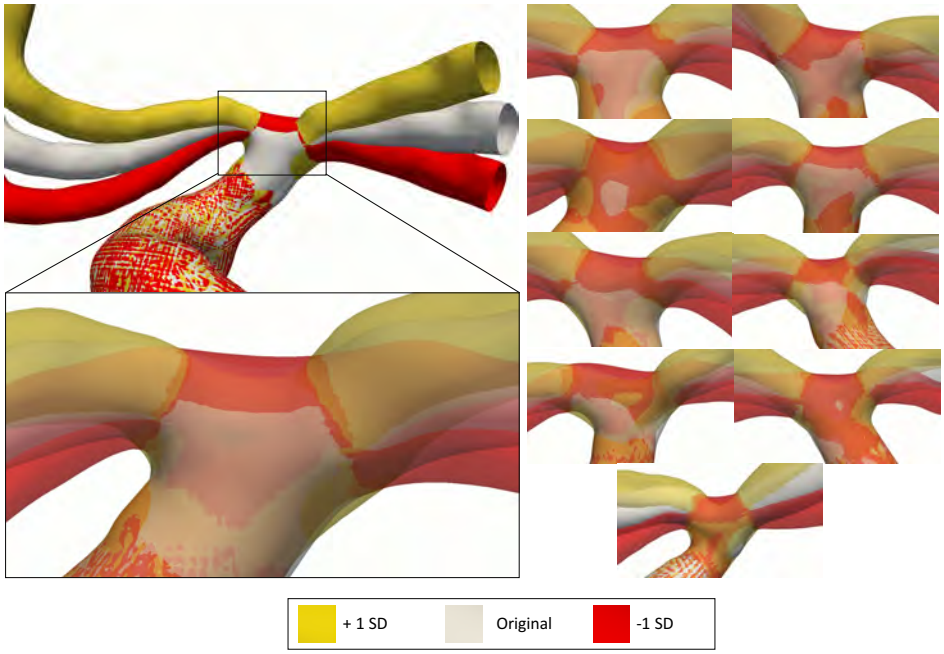

Figure 4.6: Rotation of daughter branches. The white geometries are the original surfaces, yellow are rotated upwards, and the red are rotated downwards. Each branch is rotated 18 degrees.

where **a** is the method from Ford et al. (2009) and **b** is an incremental improvement suggested in this thesis. The incremental improvement (**b**) shows an improved reconstruction of the apex for **1b-6b** and **9b**, compared to the method from Ford et al. (2009) (**a**). In the subplot **10b**, one can observe that the incremental improvement overestimates the apex of the bifurcation and creates a smoother slope than the original surface. Compared to **10a**, the reconstructed surface is also different to the original surface with a high peak curvature in the apex of the bifurcation. In case **8**, the original surface is almost identical to the approximation from Ford et al. (2009), and overestimated in **b**. For the approximation of the daughter branches, only small changes can be observed. Case 7 includes a proximal stenosis, and the estimation off the daughter branches is therefore far off for both methods in this case.

4.2.2 Objective Rotation of Daughter Branches

The standard deviation (SD) of the angle in the bifurcation is 18 degrees in the ten healthy case, which is consistent with Ingebrigtsen et al. [25]. The rotation was applied to all cases with ± one SD, and qualitative results are

presented in Figure 4.6. Looking at the leftmost part, we can see that the daughter branches are rotated to have wider and narrower angles in the bifurcation. The geometry remains unchanged before the bifurcation, and the patient-specific forms are preserved after the bifurcation. Now addressing the bifurcation, we can observe that the different surfaces change in the apex of the bifurcation. However, the difference between the original surface and the surface with narrower angles is extremely small.

4.2.3 Area Variation

In the original surfaces, the mean area variation (R) is $R = 2.78$, and the SD is 0.95. The results from six representative cases with altered area variation are presented in Figure 4.7. The comparison is between a geometry that has been altered to have decreased area variations (gray) with a geometry that has been altered to have increased area variations (red). By observing Figure 4.7, it is clear that both geometries have kept the patient-specific bends and shape. The top-left case is an extreme case where the R in the original surface is close to two. The new surface with smaller area variations therefore contains almost no changes in the area. Another extreme case is the top-middle, where the area almost does not change at all. This case has $R = 5.01$ and, to obtain R±SD, only small changes to the minimum and maximum is needed. The rest of the cases are normal, and closer to the average R.

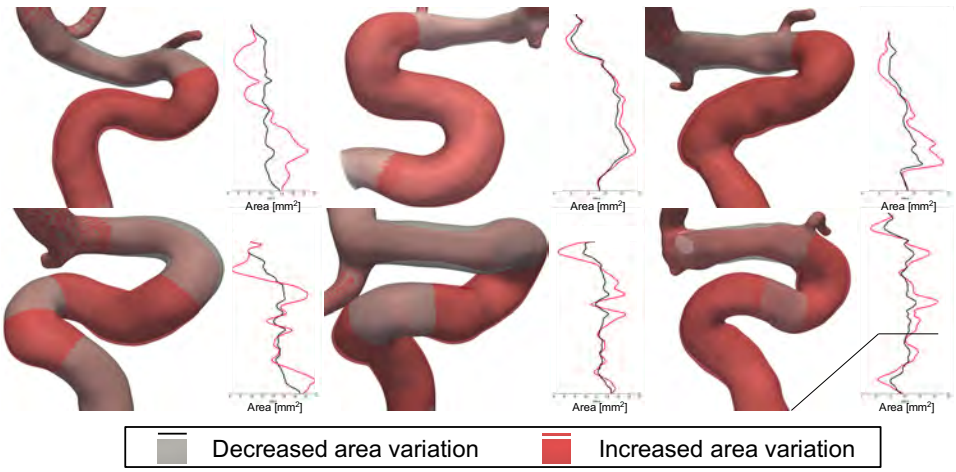

Figure 4.7: Results from six cases with varied area. The gray surface has a decreased area variation, and the red has an increased area variation. The plots next to each case is the area variation as a function of the length of the centerline.

4.3 Discussion

To ensure that the method for varying the area does not change the morphology abnormally, four additional parameters for measuring the area are suggested:

$$C = \min_s \frac{\pi r_{mis}(s)^2}{A(s)} \tag{4.8}$$

$$R_{max} = \frac{A_{max}}{A_{mean}} \tag{4.9}$$

$$R_{min} = \frac{A_{min}}{A_{mean}} \tag{4.10}$$

$$E = \max_s \left| \frac{\partial A(s)}{\partial s} \right| \tag{4.11}$$

Where r_{mis} is the radius of the minimal inscribed sphere as a function of the length of the centerline s. C provides a measurement of how similar the artery is to a perfect circle. R_{max} and R_{min} are the ratio of the minimum and maximum area over the mean area, and are an indicator of how extreme the maximum and minimum are. E is the derivative of the area with respect to the length of the centerline (s) and is a measure of the expansion or contraction along the centerline.

The results of each parameter is presented in Table 4.1 for minus one SD, the original surface, and plus one SD. From parameter C, we can observe that the altered geometries are slightly more elliptical than the original surface. However, the change is small compared to the standard deviation. Observing E, it has a slight increase with increased area variations, but the increase is negligible compared to the standard deviation. The rotation between the extremes and the mean are consistent with the changed made to the geometry. Neither the maximum, nor the minimum area, are changed abnormally. In conclusion, the area variations are patient-specific and do not change the geometry to become aberrant.

	-SD (10)	Original (10)	+SD (10)
C	0.574 ± 0.200	0.610 ± 0.185	0.560 ± 0.193
E	0.035 ± 0.034	0.043 ± 0.040	0.044 ± 0.041
R_{max}	1.280 ± 0.130	1.442 ± 0.161	1.627 ± 0.163
R_{min}	0.761 ± 0.152	0.557 ± 0.135	0.424 ± 0.120

Table 4.1: Additional parameters to measure the area variation for the altered geometries to validate the method.

	Max distance	Mean distance
Ford et al. (2009)	0.402 (0.167)	0.140 (0.124)
Incremental	0.191 (0.133)	0.096 (0.122)
p-value	**0.006**	0.429

Table 4.2: Qualitative results of the difference between the method for parent artery reconstruction in Ford et al. [91] and the incremental method presented in this thesis. There is a statistical significant improvement of the maximum distance, but the mean distance is not with so few cases. The p-value is computed with a unpaired t-test. The standard deviation is given in the parentheses.

In the study from Schimansky et al. (2013), they only observe extracranial area variations [27]. This is equivalent to stopping the changes right after the siphon. In the presented method, the area variations are altered up to the internal carotid artery terminus. This is a limitation of the method since it is not the exact same part of the artery Schimansky et al. (2013) investigated in their study. To do so would require landmarking of the geometries [93, 30]. This is left for future research. It will affect the results in the computational study, but only by increasing the observed stimuli associated with aneurysm rupture.

To check if the new method for parent artery reconstruction actually provide an improvement, we quantified the error in terms of the distance relative to the original surface in a cut plane through the bifurcation apex for both methods, respectively. The results are presented in Table 4.2, which shows that both the maximum and mean distance is minimised with the current method, although only the maximum is statistically significant. However, the standard deviation is large for the mean distance, which might indicate that there is an even better way to rebuild the bifurcation.

In computational studies of plausible hemodynamic stimuli in the bifurcation, the WSS and the WSSG is typically reported. The question then becomes: Is the reconstructed surface close enough to not affect the stimuli in the bifurcation? To check for this, the flow in all geometries used in the validation test were simulated to compare the stimuli in the bifurcation. The details of the method for these simulations are described in Section 5.3. The WSS and WSSG are presented in Figure 4.8. The indices were sampled by taking the same line as defined above and plotting the WSS over the normalized distance of the line. Observing the WSS, we can see that the general agreement is quite good in most cases for the method suggested in this thesis. However, for #8 and #9 the WSS in the original surface is different from both methods. For Ford et al. there are two additional outliers, case #4 and #5. Observing the WSSG, there is a huge difference with respect

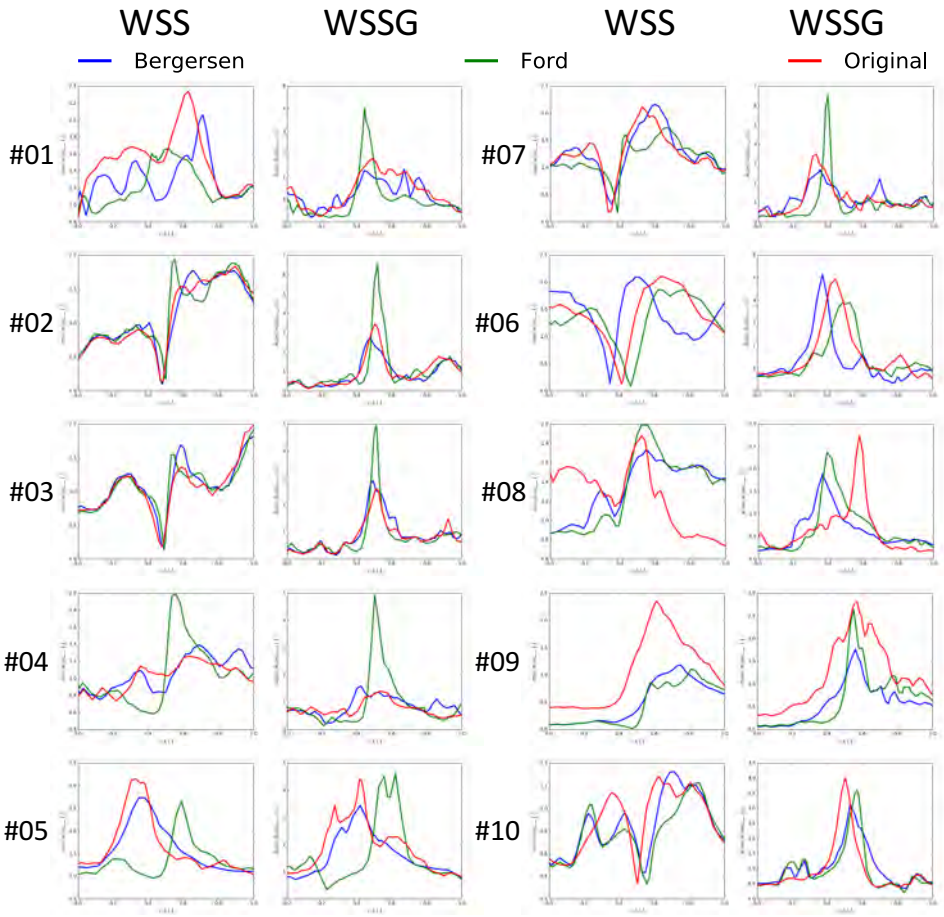

Figure 4.8: Validation of the incremental improvement for parent artery reconstruction.

to the maximum WSSG in the method of Ford et al. (2009). These results are consistent with the validation where the apex of the bifurcation shows a high peak curvature rather than a smooth surface. The overall assessment is that the reconstructed surface is close enough in both WSS and WSSG to be used in a computational study for aneurysm initiation.

In the method relating to objectively rotating the daughter branches, there is a lack of validation against bifurcations with a narrower angle. It could be that the bifurcation apex does not change enough when the branches are rotated to have a narrower angle, see Figure 4.6. This might "dampen" the real effects in the computational study.

Previous efforts to investigate the link between parent artery morphology and hemodynamic stimuli have only been limited to idealized models such as the studies from Tutucu et al. (20014) [94], and Seshadri et al. (2011) [95].

The methods presented here are not perfect, but are far more realistic then in previous studies.

4.4 Conclusion

The methods presented open up new possibilities to correlate how morphology impacts the hemodynamics in patient-specific geometries. Although admittedly not perfect, the developed tools proved a parent artery closer to the original surface. These tools will be applied in Chapter 5 to find a plausible hemodynamic stimuli for aneurysm initiation. The tools are open access, and may enable others to perform large cohort studies, or improve the tools with new methods, or apply them to other vascular beds.

Chapter 5

A Computational Study of the Link Between Morphology and Hemodynamics of the Internal Carotid Artery

The goal of this chapter is to investigate the link between morphology known to be statistically correlated with intracranial aneurysms and the hemodynamic stimuli in the terminal bifurcation of the internal carotid artery. The morphology will be altered applying the tools developed in Chapter 4. The results can offer plausible hemodynamic stimuli for aneurysm initiation. In addition, the results might shed light on the hypothesis from Valen-Sendstad et al. (2013) [20], stating that flow instabilities might play a role in aneurysm initiation, and the hypothesis from Meng et al. (2007), which states that a combination of high WSS and WSSG is the cause of aneurysm initiation.

5.1 Method

Three representative cases were chosen for this study, out of the ten healthy cases from the ANEURISK open access database. For each case, five simulations were performed: ± one standard deviation (SD) of the angles in the bifurcation, the original surface, and ± one SD of the area variation.

The inlet and outlet had to be cut in order to achieve the exact same cut perpendicular to the centerline for all variants of a case. To remove the

effects of the artificial boundary condition, flow extensions of five times the radius were added to the inlet and outlets, using *vmtkflowextensions*.

The meshes were created using *vmtk*, with approximately four million tetrahedral cells and four boundary layers. From previous studies, we know that this is a more than adequate to compute hemodynamic indices [21, 24]. The local cell size is dependent on the local surface curvature and the distance to a point, which is manually placed in the siphon. The full command used for meshing is

```
vmtksurfacecurvature -ifile case_name_distance_to_sphere.vtp -absolute 1
 ↪  -median 1 -type gaussian -reciprocal 1 -offset 0.15 --pipe
 ↪  vmtksurfacearrayoperation -iarray Curvature -i2array DistanceToSpheres
 ↪  -resultarray Size -operation multiply --pipe vmtkmeshgenerator
 ↪  -elementsizemode edgelengtharray -edgelengtharray Size -boundarylayer 1
 ↪  -sublayers 4 -boundarylayeroncaps 0 -thicknessfactor .85 -sublayerratio
 ↪  .75 -tetrahedralize 1 -volumeelementfactor 0.8 -endcapsedgelengthfactor
 ↪  1.0 --pipe vmtkmeshwriter -entityidsarray CellEntityIds -ofile
 ↪  case_name.xml --pipe vmtkmeshwriter -entityidsarray CellEntityIds
 ↪  -ofile case_name.vtu
```

One cardiac cycle is on average 0.951 s [96], therefore the time step is set to be $\Delta t = 9.51 \cdot 10^{-5}$, which is equivalent to 10 000 time steps per cardiac cycle. From previous studies using the same solver, we know that this is sufficient temporal resolution [24]. One heartbeat is equivalent to approximately five flowthroughs, and therefore each simulation is only computed for two cycles. The first cycle is simulated to remove the initial effects, and the second cycle is used to compute the hemodynamic indices. The details of the solver are presented in Chapter 2. The solver has also been used for previous studies of blood flow in intracranial arteries [22, 21, 24, 63, 20].

The simulations were performed under the assumption of rigid walls, and that blood can be modelled as a homogenous Newtonian fluid. The patient-specific flow rate (Q) were not available. From Valen-Sendstad et al. (2015) we have that the best approximation of the mean flow rates for the ANEURISK database cohort is $Q = 0.31A$, where A is the area of the inlet [97]. The wave form at the inlet is based on the wave from presented in Hoi et al. (2010) [96]. For the outlet condition, a resistance boundary condition was applied to ensure a physiological outflow division [98].

Several indices have been suggested in the literature to measure temporal varying WSS [99]. What we would like to capture here is both the change in direction and in magnitude as defined in equation (5.4), and referred to as temporal WSSG (TWSSG). To allow for comparison with Meng et al. (2007) [15], WSS and WSSG are also computed.

$$\tau = \mu \frac{\partial u}{\partial y_w}\Big|_{w=0} \tag{5.1}$$

$$WSS = \frac{1}{T}\int_0^T |\tau| \, \mathrm{d}t \tag{5.2}$$

$$WSSG = \nabla \left(\frac{1}{T}\int_0^T |\tau| \, \mathrm{d}t \right) \tag{5.3}$$

$$TWSSG = \frac{1}{T}\int_0^T \left| \frac{\partial \tau}{\partial t} \right| \mathrm{d}t \tag{5.4}$$

Where y_w is the distance to the wall, and u is the tangential velocity to the wall. To compare the results between each case all indices were normalized by the mean value in the bifurcation, as defined by Step 3 in Figure 4.3, of the original surface.

5.2 Results

5.2.1 Objective Rotation of Daughter Branches

The results of CFD simulations, using the geometries with rotated daughter branches, are presented in Figure 5.1, 5.2, and 5.3, respectivly. Figure 5.1 addresses changes in WSS due to the rotation of the daughter branches. The general trend is that the WSS in the apex of the bifurcation increases from low WSS to high WSS when going from wide angles (left pane of Figure 5.1) to narrow angles (right pane of Figure 5.1). In cases #1 and #3, the change between geometry with narrower angles (left pane of Figure 5.1) and the original surface (middle pane of Figure 5.1) is the largest.

The results from the WSSG are shown in Figure 5.2. Looking at all cases under one, high WSSG magnitude in the apex is correlated with narrower angles in the bifurcation. In particular, the surface with wider angles (left pane of Figure 5.2) has low WSSG magnitude in the apex of the bifurcation. The difference between the original surface (middle pane of Figure 5.2) and the surface with narrower angles (right pane of Figure 5.2) is that the magnitude does not increase as much, but there is a larger area of impact.

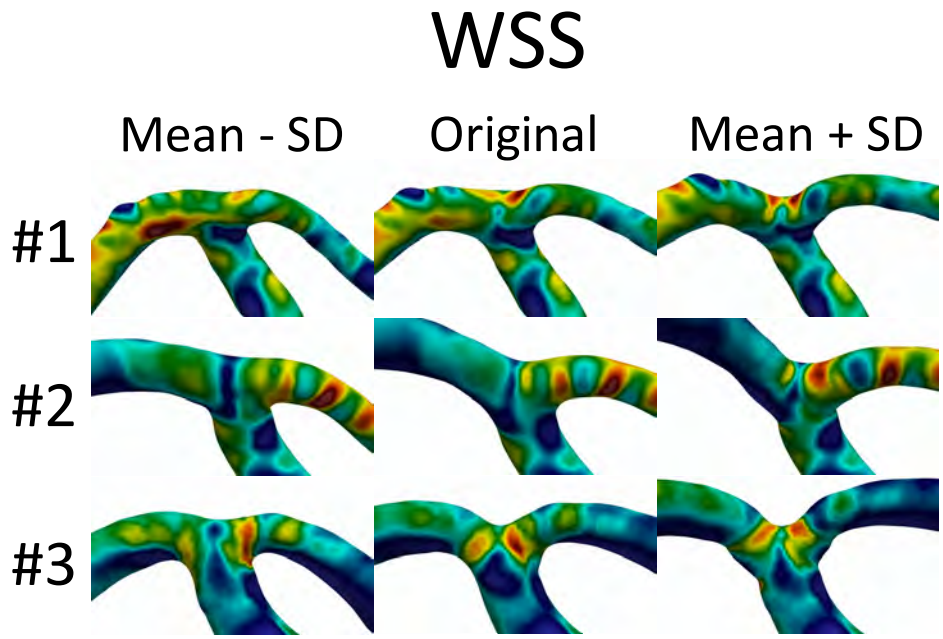

Figure 5.1: WSS for three cases, and three simulations per case, where the angles in the internal carotid terminus are changed ± one SD.

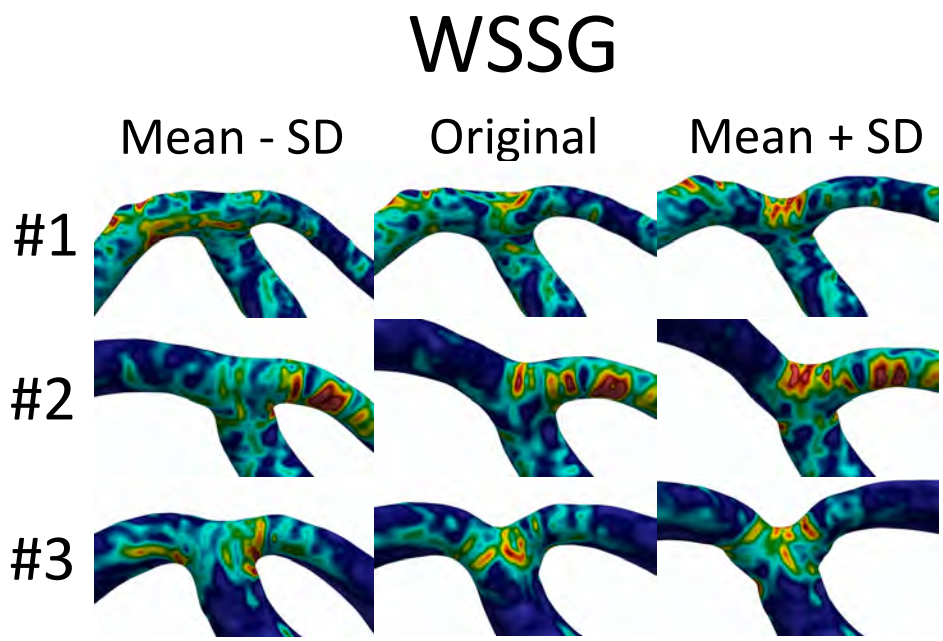

Figure 5.2: WSSG for three cases, and three simulations per case, where the angles in the internal carotid terminus are changed ± one SD.

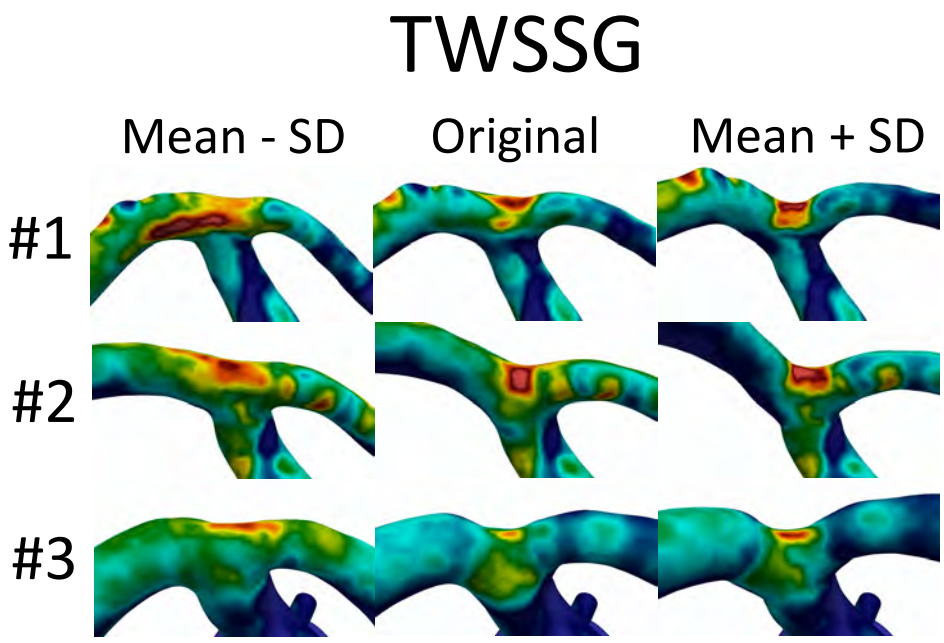

Figure 5.3: TWSSG for three cases, and three simulations per case, where the angles in the internal carotid terminus are changed ± one SD.

Lastly, for the rotated angles, we look at the TWSSG shown in Figure 5.3. The total assessment is that only the location of the impact changes, not the magnitude. It appears that only the part of the geometry that is perpendicular to the flow into the bifurcation has large TWSSG magnitude. Thus, the TWSSG is more and more confined to just the apex as the angles in the bifurcation increase. Case #3 is an exception, where the TWSSG in the original geometry is lower than in the altered surfaces.

5.2.2 Area Variations

The results from the area variations are presented in Figure 5.4, 5.5, and 5.6, respectively. We start by observing how the WSS changes when the area is varied, see Figure 5.4. The WSS for all three cases is phenotypically similar. There are only small changes in magnitude of the WSS when the area in the upstream vasculature is altered. In cases #1 and #2, the WSS upstream of the bifurcation for the surface with decreased area variation (left pane of Figure 5.4) is not equal to the original surface (middle pane of Figure 5.4). However, the WSS is equal for the original surface (middle pane of Figure 5.4 and the surface with increased area variation (right pane of Figure 5.4). In case #1, the location of the WSS changes slightly, but the magnitude is not affected. For case #3, the magnitude of the WSS is slightly lower for

the geometry with smaller area variations, but these changes are minimal.

The results for WSSG are presented in Figure 5.5. Overall, the WSSG does not change when area is varied. In case #1, the magnitude of the WSSG is slightly decreased with increasing area variations. Observing case #3, we can see that surface with decreased area variations has the maximum WSSG in the apex. This differs from the two other surfaces, where the maximum gradually moves towards the center of the bifurcation. Nevertheless, the magnitude of the WSSG does not change between the surfaces.

The results for TWSSG are presented in Figure 5.6. The difference in TWSSG between the original surface (middle pane in Figure 5.6) and the surface with increased area variation (right pane in Figure 5.6) is large in comparison to changes in WSS and WSSG. Consequently, this means that larger area variations can cause instabilities and make the temporal changes in WSS larger. The opposite seems also to be true, that smaller area variations protect from a TWSSG stimulus and causes the flow to be more stable. Case #2 does not include a change in the area of impact, but the magnitude is consistently increasing with larger area variations.

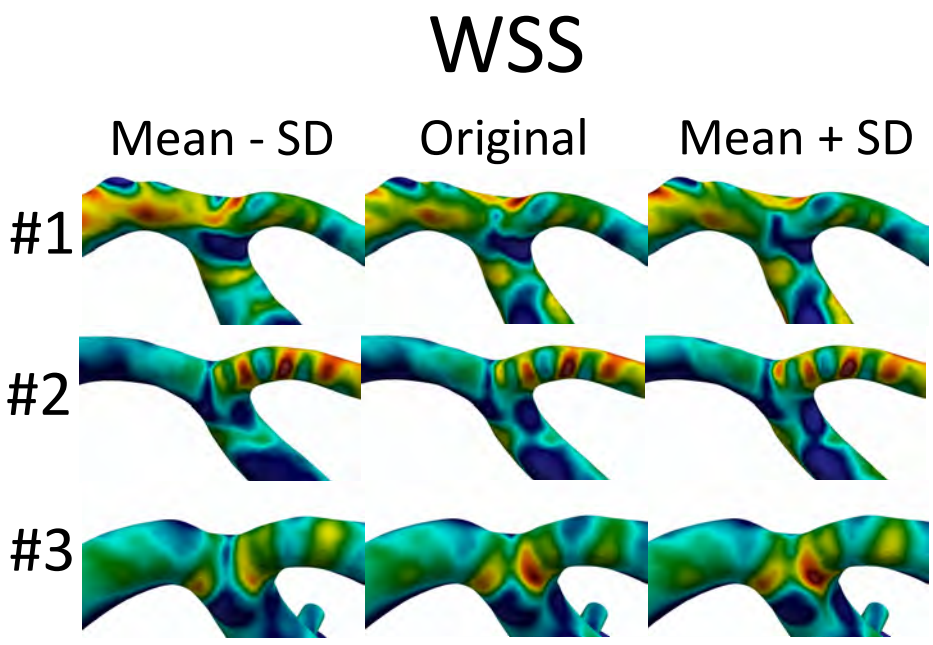

Figure 5.4: WSS for three cases, and three simulations per case, where the area variations are altered ± one SD.

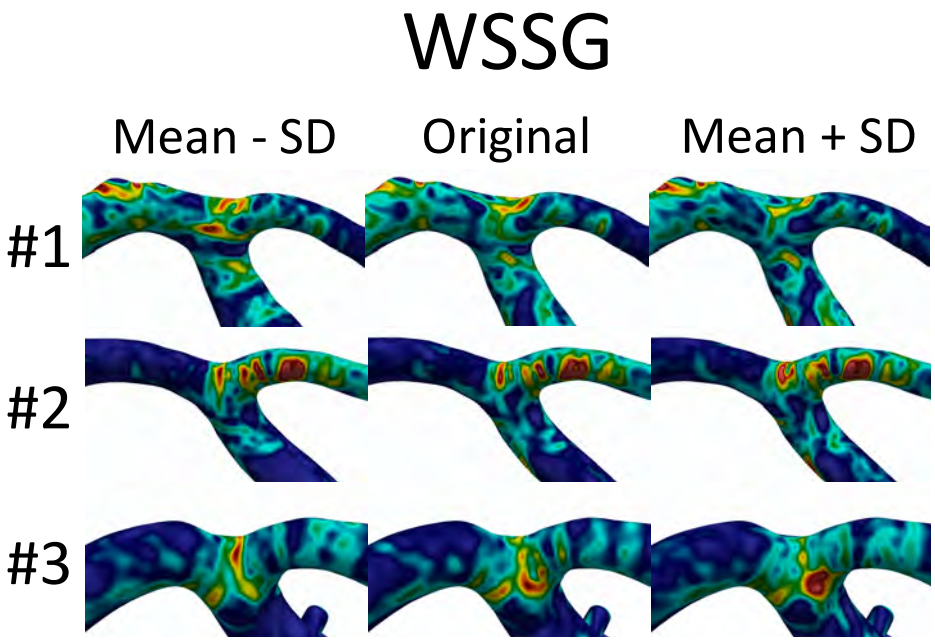

Figure 5.5: WSSG for three cases, and three simulations per case, where the area variations is altered ± one SD.

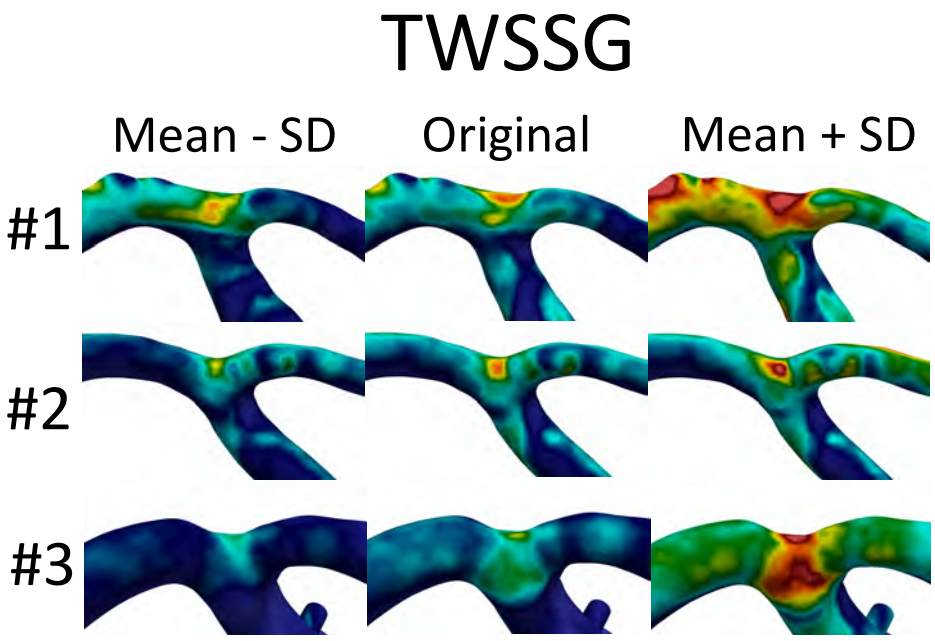

Figure 5.6: TWSSG for three cases, and three simulations per case, where the area variations is altered ± one SD.

5.3 Discussion

Only three cases were presented in the results, but additional cases have been simulated and confirmed that the presented results are representative.

5.3.1 Can the Combination of High WSS and WSSG Cause Aneurysm Initiation?

We have shown that narrower angles in the bifurcation are associated with higher WSS/WSSG and that area variations do not have an impact on WSS/WSSG. These results are in direct contradiction to the hypothesis of high WSS/WSSG from Meng et al. (2007) [15] being the cause of aneurysm initiation. For the surfaces with objectively rotated daughter branches, both WSS and WSSG are decreasing for the morphological feature that is correlated with the statistical presence of aneurysms [25]. If the combination of high WSS and WSSG was the adverse stimuli that causes adverse remodeling of the artery wall, then aneurysms should be present in geometries with narrow angles, not wide.

When varying the area, there are practically no changes in the WSS and WSSG in the apex of the bifurcation. Although the WSS and WSSG remain unchanged, the flow is phenotypically different, which can be observed in the TWSSG. Thus, WSS and WSSG fail to account for the altered stimuli that occur when the geometry is changed according to the morphological feature correlated with statistical presence in aneurysm initiation. From these results, it is unlikely that the theory from Meng et al. (2007) is valid [15].

The current results do not support the hypothesis of high WSS and WSSG being correlated with aneurysm initiation. What do previous findings indicate? 87% of all intracranial aneurysms are located in vicinity of the first two branches after carotid canal, and are located in bifurcations [100]. A theory that describes aneurysm initiation has to provide an explanation that is specific to bifurcations as well as the two first segments after the carotid canal. High WSS/WSSG is more or less specific to bifurcations, but WSS and WSSG are present in every bifurcation in the entire cardiovascular system. It is then hard to imagine that this is the stimuli cause aneurysm initiation.

If we assume that the results in this study are correct, is there a reason why the study from Meng et al. (2007) draws another conclusion? Although briefly addressed in the introduction, let us recap the setup in the experiments on which the hypothesis of high WSS and WSSG is based: *" (...) a set of experiments in rabbits and canines. With a surgical procedure, the flow rates were increased to induce aneurysm initiation (...). In the study*

from Metaxa et al. (2010), this caused the flow rates to increase on average by 325% and cause aneurysm initiation in the test subjects [16]. Based on the CFD simulations on the subject specific geometries, see Figure 1.2C and D, the authors concluded that the combination of WSS and WSSG is a dangerous stimulus that can cause aneurysm initiation". This experiment has, a posteriori, two major limitations. *Firstly* the conclusion was based on using rabbits and canines as model organisms, and the results might not be directly translated into human physiology. *Secondly*, the CFD solver used has later been shown by Khan et al. (2015) to be insufficient to capture possible flow instabilities [24]. Addressing the first limitation: the induced flow rates in the model organisms are not similar to those in the human brain. A computational study including 59 New-Zealand white rabbits showed that both the Reynolds number and the morphology of the intracranial arteries are similar to those in a humans [101]. If the Reynolds number is equal for humans and rabbits, is then a 325% increase in flow rates physiological for humans? During peak exercise, the cardiac output in human is increased with ∼250%[102], but the human brain will at maximum only have a 23% increase in flow rates in the internal carotid artery [103, 102]. Furthermore, as this blood has lower pH levels due to increased carbon dioxide in the blood, the vessels will also widen, most likely to preserve constant WSS [103]. Since the WSS scales with approximately Q/D^3 in a pipe [104] we have that the new radius is ∼7% larger. The altered radius and the increased flow rates will give an ∼15% increase in Reynolds number. In the experiments, it is not mentioned how the diameter changes, as it is only measured before the surgery. However, if we assume that the blood vessels adapted to obtain a constant WSS, the Reynolds number increases by ∼220%. Thus, the increased flow rates led to a unphysiological Reynolds number which we would never find in the human brain. This is closely connected to the second limitation of experiments. In light of the results from Valen-Sendstad et al. (2013), two separate studies by Valen-Sendstad et al. (2014) and Khan et al. (2015) have shown that the combination of solver, mesh size and Δt used in most CFD studies of intracranial aneurysms are insufficient to resolve the flow and detect flow instabilities. Since flow instabilities are detected in the normal range of Reynolds numbers, one would expect that an over 200% increase in Reynolds number would cause the flow to be highly unstable. From preliminary results presented by Valen-Sendstad et al. (2015) at the *Computational Fluid Dynamics (CFD) in Medicine and Biology II* conference in Albufeira, Portugal, we know that even a doubling of the flow rates, and using a standard solver with default settings found in the aneurysm literature, will not make the result unstable, but only result in higher WSS and WSSG [105]. The combination of the two limitations provides a possible explanation for why results from Meng et al. (2007) are possibly misleading.

5.3.2 Can Flow Instabilities Cause Aneurysm Initiation?

The results for TWSSG are inconclusive, but TWSSG can be a plausible stimulus for aneurysm initiation. For the surfaces with objectively rotated daughter branches, the magnitude does not change when the morphology is altered. However, the area of impact decreased with narrower angles. In the geometries with altered area variations, there is a clear correlation between increased TWSSG and the morphological features associated with the presence of aneurysms. At this point, the hypothesis of TWSSG offers a more plausible explanation [20].

A possible explanation for the lack of correlation in geometries with angle variations can be found in Figure 4.5 and Figure 4.6: bifurcations with smaller angles might be overestimated at the apex with the suggested method. In the results from the comparison between the original surface and the reconstructed surface, there are four models that are overestimated. These models are (in retrospect) found to have a narrower angle in the bifurcation. In addition, in Figure 4.6, one can observe that the model with narrower angles in the bifurcation does not change in the apex. If the apex in the bifurcation was not perpendicular to the flow direction at all, then there would be significantly less TWSSG. However, this is only speculative and should be confirmed by validating the method for parent artery reconstruction for narrower angles in the bifurcation.

The area variations might be overestimated since the models are altered intracranially as well as extracranially. The study from Schimansky et al. [27] that motivated to investigate area variations only referred to the extradural area variations. Therefore, the TWSSG are likely overestimated. However, upon analyzing the results, one can observe flow instabilities extradurally as well. It is likely that the same trend would be observed if the geometries were only changed extradurally.

The results from Meng et al. (2007) cannot easily explain for why 87% of aneurysms are located in the first two bifurcations after the carotid canal. Is there an explanation for this with respect to flow instabilities? In general, the blood flow in the body is laminar, but the flow in the internal carotid artery has shown to be unstable [20]. If it is a fluctuating WSS signal that causes aneurysm initiation, then one would expect that the flow instabilities only exist in this region of the brain. How quickly flow instabilities dissipate depends on the Reynolds number. To estimate how the Reynolds number changes after an bifurcation, let's consider a fully symmetric bifurcation with two daughter branches with equal radius, $r_1 = r_2 = r_d$, and a parent artery with a radius r_{PA}. Assuming that Murray's law [106] is valid, we obtain the following

$$
\begin{aligned}
r_{PA}^3 &= 2r_d^3 \\
\frac{r_{PA}}{r_d} &= 2^{\frac{1}{3}}
\end{aligned} \tag{5.5}
$$

Since the bifurcation is fully symmetric we have that

$$
Q_{PA} = \frac{1}{2} Q_d \tag{5.6}
$$

Combining (5.5) and (5.6) we can find the velocity in the daughter branch

$$
\frac{Q_d}{Q_{PA}} = \frac{A_d u_d}{A_{PA} u_{PA}} = \frac{1}{2} \tag{5.7}
$$

$$
\begin{aligned}
\frac{u_d}{u_{PA}} &= \frac{1}{2} \frac{A_{PA}}{A_d} \\
&= 2^{-1} \left(\frac{r_{PA}}{r_1} \right)^2 \\
&= 2^{-\frac{1}{3}}
\end{aligned} \tag{5.8}
$$

Now using both (5.5) and (5.8) we can approximate how the Reynolds number changes after a bifurcation

$$
\frac{Re_d}{Re_{PA}} = \frac{\frac{D_d u_d}{\nu}}{\frac{D_{PA} u_{PA}}{\nu}} \tag{5.9}
$$

$$
= \frac{r_d}{r_{PA}} \frac{u_d}{u_{PA}} \tag{5.10}
$$

$$
= 2^{-\frac{2}{3}} \approx 0.63 \tag{5.11}
$$

Hence, for each bifurcation, the Reynolds number is reduced with approximately 60%, and thus the initial instabilities from the siphon will dissipate quickly. In the vicinity of Circle of Willis Murray's law may scale with two instead of three [25, 107]. If this is true, the Reynolds number is reduced with ∼70% for each bifurcation. The Reynolds number during peak systole in the internal carotid artery is ∼500 in humans [20]. The flow instabilities will therefore stabilize quickly. This is a moderate estimate, as it does not account for the decreased flow rates due to the smaller branches that are present along larger the arteries [108]. This might provide an explanation for why ∼90% of aneurysms are located in the vicinity of the internal

carotid artery. The last ∼10% of all intracranial aneurysms are located in the basilar artery. Although several computational studies have been performed on patient-specific geometries of the basilar artery [109, 110], to the author's knowledge, none have included the vasculature down to the vertebral artery. It is challenging to obtain good images of the vertebral artery [111], and therefore to include it in computational studies. However, using idealized glass models and steady state flow, Stehbens (1985) found flow instabilities in the junction of the vertebral arteries down to Reynolds number 300 [112]. Thus, there *might* also be flow instabilities in the basilar artery as well. Based on this, we can not confirm nor reject the theory.

There are additonal morphological parameters associated with the presence of aneurysms: torsion and peak curvature [113, 114, 30]. Both curvature and torsion have been investigated in an idealized model by Lee et al. (2008), using a spectral element solver. They found that for conditions mimicking blood flow in the brain, a higher peak curvature in combination with torsion is associated with flow instabilities [115]. Although the results are not from patient-specific geometries, this supports the theory of TWSSG being the cause of aneurysm initiation.

The TWSSG is not a mathematical derived formula, it is simply a suggested index to measure changes of the direction and magnitude of WSS in time. The observed WSS signal is fluctuating in magnitude and direction, which is the important message here. There might be parameters that better measure the differences, such as oscillatory shear index (OSI), or other parameters that measure the change of direction in WSS.

To compute the velocity fields on a computer is one thing, but what happens to the actual biology of the blood vessel when exposed to a turbulent flow? Human brain arteries are muscular arteries and consist of three layers: the outer tunica adventitia, the tunica media, and the inner layer tunica intima [116]. As outlined in Chapter 1 *Introduction and Medical Background*, the inner layer consists mostly of endothelial cells, which regulate how the blood vessels adapt to a changing hemodynamic environment. Under normal conditions, where laminar blood flow acts on the endothelial cells, they maintain a healthy structure and alignment [117]. However, for a transient or turbulent flow, it has been shown that the turnover of endothelial cells is increased [118]. The increased turnover impairs the production of nitric oxide, which is an important cellular signaling molecule for regulation of the size of the blood vessels [119]. Thus, leaving the blood vessel vulnerable for inflammation and adverse remodeling, which might cause abnormalities such as aneurysms. Another important inhibitor for inflammation in the blood vessel is the transcription factor Krüppel-like factor 2 (KLF2) which is, amongst other, found in the endothelial layer of the blood vessel. An increased expression of KLF2 inhibits inflammation in the blood vessel [120].

The KLF2 is regulated by the local hemodynamic environment and its expression is increased for a laminar flow and decreased for a disturbed, or turbulent flow [121, 122]. From *in vivo* experiments in mice, where the diameter of a mouse aorto-caval arteriovenous fistula[1] was manipulated to alter the WSS stimuli, Yamamoto et al. (2015) found that the frequency of the WSS was more important for controlling KLF2 levels than the magnitude [122]. Hence, increased high-frequent instabilities led to downregulation of KLF2. However, mice have been shown to be a poor model organism for investigating human inflammatory diseases [123], so this result can not be blindly translated into human physiology. In addition, the shear stress in an animal is highly dependent on the of size and body mass [124]. The above discussion of *"what happens to the actual biology of the blood vessel when exposed to a turbulent flow"* is superficial, but the current knowledge of how mechanotransduction is affected when the WSS is multidirectional is limited. Although more research is needed, a fluctuating WSS signal is likely to be unhealthy and proinflammatory. New insight into the effects of multidirectional WSS is important for understanding the complete pathophysiology of aneurysms and the mechanotransduction pathways leading to aneurysm initiation.

5.3.3 Model Assumptions

When performing an imaged based computational study of aneurysm initiation, several assumptions are made. Three of these assumptions will be discussed: inlet flow rates, non-Newtonian rheology, and rigid walls.

For computational studies to be comparable, the same assumptions have to be applied. Most CFD studies of blood flow in aneurysms do not report the flow rates applied. However, the two most commonly reported parameters are constant flow rates $Q \sim D^0$ [14] and constant WSS at the inlet $Q \sim D^3$ [13]. Although the mean flow rate for a group of patients may be the same, the inlet velocity would drastically change when the diameter is different than the mean. Let us consider a case where $D << D_{mean}$, then the velocity for constant flow rates would be high, whereas the velocity for constant WSS would be low. For a case with a large diameter, the velocity would be opposite, high for constant WSS and low for constant flow rates. For this study we applied $Q = 0.31A$ as an inlet condition, and this is based on one of the only studies comparing different flow rates assumptions for intracranial blood flow [97]. A study from Marzo et al. (2011) tested the effect of patient-specific flow rates comparing different modeled inflow conditions, and found that the WSS changed significantly. However, when looking at the

[1] An arteriovenous fistula is when an artery goes directly into a vein without going through the capillaries.

normalized values, the WSS are, for all practical purposes, identical [125]. In addition, the results in the study from Marzo et al. (2011) [125] were based on a solution strategy which is not able to capture flow instabilities, and results should be reproduced to check if this can impact the flow phenotype.

The second assumption was that blood can be modeled as a Newtonian fluid. In a study from Xiang et al. (2011) they investigated the impact of Newtonian rheology in three aneurysms, and found only a significant difference in a very slow recirculating flow in the aneurysm, but no effect in the rest of the model [126]. These results are later confirmed by Castro et al. (2014), investigating the effect in eight patients, and found no statistically significant changes in WSS when assuming Newtonian rheology [127].

The third, and final, assumption was that the blood vessel walls are rigid and not compliant. Previous studies using fluid structure interaction (FSI) solvers to model the effect of a compliant wall found an effect up to 50% in WSS in the aneurysm. Taking a closer look at the data presented, the 50% difference in WSS is for a point value comparison, and the changes in WSS due to a compliant geometry are in general negligible. Moreover, the maximum difference were found in the aneurysm, and no difference were found in the artery [128, 129]. The geometries used in this thesis do not include aneurysms. Thus, the assumption of rigid walls should not effect the solution.

5.3.4 Limitations

The study described here has three limitations 1) the results are qualitative and not quantitative, 2) the number of simulations is limited, and 3) lifestyle, genetics and perivascular environment is not discussed or taken into account. The first two limitations are highly connected as they are all dependent on additional time. The third and final limitation is a more general limitation of all CFD studies, as there is often a limited amount of information available about the patients.

5.4 Conclusion

From the results and the following discussion, we show that combination of high WSS and WSSG is not correlated with morphological features that are associated with aneurysms. Therefore, it might not be the stimuli causing aneurysm initiation.

Additional efforts are needed to contradict or confirm that TWSSG is an adverse stimulus that can cause aneurysm initiation. A first step would be to

perform a large case study using a validated tool for manipulating patient-specific morphology. A final test would be to understand the mechanotransduction pathways that are activated during multidirectional flow from both *in vivo* and *in vitro* experiments.

Chapter 6

Lessons Learned and Future Directions

The results from the U.S. Food and Drug Administration's benchmark challenge in Stewart et al. (2012) [52] presented in Chapter 3 *Verification and Validation* illustrate how difficult it can be to compute CFD of such a simple geometry. There was a large intervariability between the groups. Additionally, our computations of the same challenge resulted in a phenotypically different flow for the transitional cases. This is not unique for this challenge. Peng et al. (2016) published the results of a similar challenge intended for validation in indoor environment computations. The goal of the challenge was to investigate the error introduced by the user in choice of boundary conditions, mesh, time steps, convergence, turbulence model, discretization, etc. The problem set-up was the classical backward facing step with an uninvestigated ratio of the inlet and the step, and over a range of Reynolds numbers (1 - 10000). The results varied between the groups, even for low Reynolds numbers. The max coefficient of variance was over 50%, and the largest error compared to the mean was over 150%. Even for groups that claimed to have applied the same methods, there were large variations in the reported results [130]. Combining the results from this challenge with the results published in the study by Stewart et al. (2012) [52] and our own results, it is clear that CFD is highly user-dependent. Each scientific community that extensively uses CFD have to agree upon some well-defined standards to insure that the studies are user-independent. The lesson learned is that CFD is not a fully developed and ready to use "push-button" tool.

Challenges as the ones described above are a good way to investigate which parameters or assumptions have an impact on the solution. The challenge launched by Steinman et al. (2013) investigated the user-dependency when computing the velocity field and pressure drop in a giant aneurysm. Be-

tween the 25 participants there was a large variability in the velocity field in the aneurysm, and only some groups reported flow fluctuations in the aneurysm [131]. A following challenge was launched by Kono et al. (2015) (www.cfdchallenge2015.com), but so far only preliminary results have been presented at the *Summer Biomechanics, Bioengineering and Biotransport Conference* (SB^3C), June 2015, Utah. The 28 CFD participants were only given five DICOM images, and asked to predict rupture status, in other words, a real-life test. The same data were given to 231 clinicians who were also asked to predict rupture based on morphology. Each group had to segment the DICOM image, choose how much of the geometry to include, create a mesh, choose inlet condition, flow rates, outlet conditions and so on. Preliminary results presented at the SB^3C in 2015 showed that the experienced CFD groups had a significantly better rupture prediction (84%) than the clinicians (64%). However, looking at the flow simulations, there was an extremely large intervariability. The simulations were phenotypically different and there was no consistency in the choice of flow rates, segmentation, inlet conditions, and outlet conditions [132]. When the results have been properly analyzed and published, this will hopefully challenge and force the aneurysm community to converge to a common set of rules for CFD simulations of blood flow in intracranial arteries.

The results from the computational study in this thesis indicate how CFD could provide misleading a hemodynamic stimulus. Previous studies should be revisited in light of these results. If the original study from Meng et al. (2009) [15] had done proper *verification and validation* of their solver, the results could have been different. Furthermore, this highlights the importance that all new studies have to provide a sufficient amount of information about the following: discretization, solver parameters and convergence, mesh resolution, time steps, inflow conditions, flow rates, outlet conditions, and how the surface was segmented and potentially smoothed, and finally, how the medical images were obtained. Without reporting these parameters, the results are not reproducible.

To sum up, the lack of standardization and *verification and validation* are taking the focus and research effort away from advancing the field and unraveling the complexity of biomedical problems.

We are currently in the process of writing up the studies as journal papers. The results from Section 3.2 will be published in collaboration with my thesis supervisors with additional results from a spectral element solver and linear stability analysis. From Chapter 4, the goal is to publish two papers, one where the incremental improvement to aneurysm removal is presented, validated, and applied on bifurcation aneurysms. The second paper will present and validate tools for rotation of daughter branches, area variation, improved landmarking, and curvature. Although both landmarking and

curvature are not presented here, initial efforts have been made to implement these as well. From Chapter 5, a study applying the tools presented in Chapter 4 will be used to authoritatively falsify the theory of high WSS and WSSG being the hemodynamic stimuli that can cause aneurysm initiation. In total, four papers will hopefully be published from the work in this thesis, in addition to the already accepted refereed proceedings.

Chapter 7

Conclusions

The main findings of this thesis are:

- CFD is not a "push-button" tool that is automatically validated for all applications, and the lack of *verification and validation* can cause misleading results.
- New tools to objectively alter morphological features are presented to rotate the daughter branches in the bifurcation and vary the area in an artery.
- An incremental improvement of the method presented in Ford et al. (2014) [91] for aneurysm removal is introduced.
- The combination of high WSS and WSSG is not correlated with morphological features that are associated with aneurysms, and thus might not be the cause of aneurysm initiation.
- Flow instabilities might be the cause of aneurysm initiation, but further research is needed to confirm this.

Bibliography

[1] Naghavi M, Wang H, Lozano R, Davis A, Liang X, Zhou M, et al. Global, regional, and national age-sex specific all-cause and cause-specific mortality for 240 causes of death, 1990-2013: a systematic analysis for the Global Burden of Disease Study 2013. The Lancet. 2015;385(9963):117–171.

[2] Yusuf S, Reddy S, Ôunpuu S, Anand S. Global burden of cardiovascular diseases part I: general considerations, the epidemiologic transition, risk factors, and impact of urbanization. Circulation. 2001;104(22):2746–2753.

[3] Lantigua H, Ortega-Gutierrez S, Schmidt JM, Lee K, Badjatia N, Agarwal S, et al. Subarachnoid hemorrhage: who dies, and why? Critical Care. 2015;19(1):1–10.

[4] van Gijn J, Kerr RS, Rinkel GJ. Subarachnoid haemorrhage. The Lancet. 2007;369(9558):306–318.

[5] Suarez JI, Tarr RW, Selman WR. Aneurysmal subarachnoid hemorrhage. New England Journal of Medicine. 2006;354(4):387–396.

[6] Canham P, Finlay H, Tong S. Stereological analysis of the layered collagen of human intracranial aneurysms. Journal of Microscopy. 1996;183(2):170–180.

[7] ACROSS Group and others. Epidemiology of aneurysmal subarachnoid hemorrhage in Australia and New Zealand incidence and case fatality from the Australasian Cooperative Research on Subarachnoid Hemorrhage Study (ACROSS). Stroke. 2000;31(8):1843–1850.

[8] Johnston SC, Selvin S, Gress DR. The burden, trends, and demographics of mortality from subarachnoid hemorrhage. Neurology. 1998;50(5):1413–1418.

[9] Morita A, Kirino T, Hashi K, Aoki N, Fukuhara S, Hashimoto N, et al. The natural course of unruptured cerebral aneurysms in a Japanese

cohort. The New England Journal of Medicine. 2012;366(26):2474–2482.

[10] Wermer MJ, Kool H, Albrecht KW, Rinkel GJ, Aneurysm Screening after Treatment for Ruptured Aneurysms Study Group and others. Subarachnoid hemorrhage treated with clipping: long-term effects on employment, relationships, personality, and mood. Neurosurgery. 2007;60(1):91–98.

[11] Cebral JR, Raschi M. Suggested connections between risk factors of intracranial aneurysms: a review. Annals of Biomedical Engineering. 2013;41(7):1366–1383.

[12] Cebral JR, Castro MA, Burgess JE, Pergolizzi RS, Sheridan MJ, Putman CM. Characterization of cerebral aneurysms for assessing risk of rupture by using patient-specific computational hemodynamics models. American Journal of Neuroradiology. 2005;26(10):2550–2559.

[13] Cebral JR, Mut F, Weir J, Putman CM. Association of hemodynamic characteristics and cerebral aneurysm rupture. American Journal of Neuroradiology. 2011;32(2):264–270.

[14] Xiang J, Natarajan SK, Tremmel M, Ma D, Mocco J, Hopkins LN, et al. Hemodynamic–morphologic discriminants for intracranial aneurysm rupture. Stroke. 2011;42(1):144–152.

[15] Meng H, Wang Z, Hoi Y, Gao L, Metaxa E, Swartz DD, et al. Complex hemodynamics at the apex of an arterial bifurcation induces vascular remodeling resembling cerebral aneurysm initiation. Stroke. 2007;38(6):1924–1931.

[16] Metaxa E, Tremmel M, Natarajan SK, Xiang J, Paluch RA, Mandelbaum M, et al. Characterization of critical hemodynamics contributing to aneurysmal remodeling at the basilar terminus in a rabbit model. Stroke. 2010;41(8):1774–1782.

[17] Meng H, Swartz DD, Wang Z, Hoi Y, Kolega J, Metaxa EM, et al. A model system for mapping vascular responses to complex hemodynamics at arterial bifurcations in vivo. Neurosurgery. 2006;59(5):1094.

[18] Wang Z, Kolega J, Hoi Y, Gao L, Swartz DD, Levy EI, et al. Molecular alterations associated with aneurysmal remodeling are localized in the high hemodynamic stress region of a created carotid bifurcation. Neurosurgery. 2009;65(1):169.

[19] Tremmel M, Xiang J, Hoi Y, Kolega J, Siddiqui AH, Mocco J, et al. Mapping vascular response to in vivo hemodynamics: application to increased flow at the basilar terminus. Biomechanics and modeling in mechanobiology. 2010;9(4):421–434.

[20] Valen-Sendstad K, Mardal KA, Steinman DA. High-resolution CFD detects high-frequency velocity fluctuations in bifurcation, but not sidewall, aneurysms. Journal of Biomechanics. 2013;46(2):402–407.

[21] Valen-Sendstad K, Steinman DA. Mind the gap: impact of computational fluid dynamics solution strategy on prediction of intracranial aneurysm hemodynamics and rupture status indicators. American Journal of Neuroradiology. 2014;35(3):536–543.

[22] Valen-Sendstad K, Piccinelli M, Steinman DA. High-resolution computational fluid dynamics detects flow instabilities in the carotid siphon: implications for aneurysm initiation and rupture? Journal of Biomechanics. 2014;47(12):3210–3216.

[23] Roache PJ, Ghia KN, White FM. Editorial policy statement on the control of numerical accuracy. Journal of Fluids Engineering. 1986;108(1):2–3.

[24] Khan M, Valen-Sendstad K, Steinman D. Narrowing the expertise gap for predicting intracranial aneurysm hemodynamics: impact of solver numerics versus mesh and time-step resolution. American Journal of Neuroradiology. 2015;36(7):1310–1316.

[25] Ingebrigtsen T, Morgan MK, Faulder K, Ingebrigtsen L, Sparr T, Schirmer H. Bifurcation geometry and the presence of cerebral artery aneurysms. Journal of Neurosurgery. 2004;101(1):108–113.

[26] Ho AL, Lin N, Frerichs KU, Du R. Intrinsic, transitional, and extrinsic morphological factors associated with rupture of intracranial aneurysms. Neurosurgery. 2015;77(3):433–442.

[27] Schimansky S, Patel S, Rahal J, Lauric A, Malek AM. Extradural internal carotid artery caliber dysregulation is associated with cerebral aneurysms. Stroke. 2013;44(12):3561–3564.

[28] Sangalli LM, Secchi P, Vantini S, Veneziani A. A case study in exploratory functional data analysis: geometrical features of the internal carotid artery. Journal of the American Statistical Association. 2009;104(485):37–48.

[29] Lauric A, Hippelheuser J, Safain MG, Malek AM. Curvature effect on hemodynamic conditions at the inner bend of the carotid siphon and its relation to aneurysm formation. Journal of Biomechanics. 2014;47(12):3018–3027.

[30] Piccinelli M, Bacigaluppi S, Boccardi E, Ene-Iordache B, Remuzzi A, Veneziani A, et al. Geometry of the internal carotid artery and recurrent patterns in location, orientation, and rupture status of lat-

eral aneurysms: an image-based computational study. Neurosurgery. 2011;68(5):1270–1285.

[31] White FM. Viscous fluid flow. vol. 3. McGraw-Hill New York; 2006.

[32] Fefferman CL. Existence and smoothness of the Navier-Stokes equation. The millennium prize problems. 2000;p. 57–67.

[33] Pope SB. Turbulent flows. Cambridge university press; 2000.

[34] Mortensen M, Valen-Sendstad K. Oasis: A high-level/high-performance open source Navier-Stokes solver. Computer Physics Communications. 2015;188:177–188.

[35] Simo J, Armero F. Unconditional stability and long-term behavior of transient algorithms for the incompressible Navier-Stokes and Euler equations. Computer Methods in Applied Mechanics and Engineering. 1994;111(1):111–154.

[36] Brown DL, Cortez R, Minion ML. Accurate projection methods for the incompressible Navier-Stokes equations. Journal of Computational Physics. 2001;168(2):464–499.

[37] Langtangen HP, Mardal KA, Winther R. Numerical methods for incompressible viscous flow. Advances in Water Resources. 2002;25(8):1125–1146.

[38] Oberkampf WL, Roy CJ. Verification and validation in scientific computing. Cambridge University Press; 2010.

[39] Jakobsen B, Rosendahl F. The Sleipner platform accident. Structural Engineering International. 1994;4(3):190–193.

[40] Oberkampf WL, Trucano TG. Verification and validation benchmarks. Nuclear Engineering and Design. 2008;238(3):716–743.

[41] Dijkstra EW. A discipline of programming. vol. 1. Prentice-Hall Englewood Cliffs; 1976.

[42] Knupp P, Salari K. Verification of computer codes in computational science and engineering. CRC Press; 2002.

[43] Roache PJ. Verification and Validation in Computational Science and Engineering. Hermosa; 1998.

[44] Roache PJ. Code verification by the method of manufactured solutions. Journal of Fluids Engineering. 2002;124(1):4–10.

[45] SymPy Development Team. SymPy: Python library for symbolic mathematics; 2014. Available from: `http://www.sympy.org`.

[46] Mortensen M, Bergersen A. Oasis forked from mikaem/Oasis; 2016. Accessed: 2016-15-03. Web Site. Available from: `https://github.com/aslakbergersen/Oasis`.

[47] Guillén-González F, Tierra G. Superconvergence in velocity and pressure for the 3D time-dependent Navier-Stokes equations. SeMA Journal. 2012;57(1):49–67.

[48] of Aeronautics AI, Staf A. AIAA Guide for the Verification and Validation of Computational Fluid Dynamics Simulations. American Institute of Aeronautics & Astronautics; 1998.

[49] Marvin JG. Perspective on computational fluid dynamics validation. AIAA journal. 1995;33(10):1778–1787.

[50] Sargent RG. Verification and validation of simulation models. In: Proceedings of the 37th conference on Winter simulation. Winter Simulation Conference; 2005. p. 130–143.

[51] Valen-Sendstad K, Mortensen M. Validation and verification of Oasis, an open-source high-preformance FEniCS/FEM-based CFD solver. Computer Physics Communications. Manuscript in preparation;.

[52] Stewart SF, Paterson EG, Burgreen GW, Hariharan P, Giarra M, Reddy V, et al. Assessment of CFD performance in simulations of an idealized medical device: results of FDA's first computational interlaboratory study. Cardiovascular Engineering and Technology. 2012;3(2):139–160.

[53] Bhushan S, Walters DK, Burgreen GW. Laminar, turbulent, and transitional simulations in benchmark cases with cardiovascular device features. Cardiovascular Engineering and Technology. 2013;4(4):408–426.

[54] Janiga G. Large eddy simulation of the FDA benchmark nozzle for a Reynolds number of 6500. Computers in Biology and Medicine. 2014;47:113–119.

[55] Delorme YT, Anupindi K, Frankel SH. Large eddy simulation of FDA's idealized medical device. Cardiovascular Engineering and Technology. 2013;4(4):392–407.

[56] Passerini T, Quaini A, Villa U, Veneziani A, Canic S. Validation of an open source framework for the simulation of blood flow in rigid and deformable vessels. International Journal for Numerical Methods in Biomedical Engineering. 2013;29(11):1192–1213.

[57] Hariharan P, Giarra M, Reddy V, Day SW, Manning KB, Deutsch S, et al. Multilaboratory particle image velocimetry analysis of the

FDA benchmark nozzle model to support validation of computational fluid dynamics simulations. Journal of Biomechanical Engineering. 2011;133(4):041002 1–14.

[58] Mortensen M. Tools; 2016. Accessed: 2016-15-03. Web Site. Available from: `https://github.com/mikaem/tools`.

[59] Mortensen M. Fenicstools; 2016. Accessed: 2016-15-03. Web Site. Available from: `https://github.com/mikaem/fenicstools`.

[60] Welch PD. The use of fast Fourier transform for the estimation of power spectra: a method based on time averaging over short, modified periodograms. IEEE Transactions on Audio and Electroacoustics. 1967;15(2):70–73.

[61] Kolmogorov AN. The local structure of turbulence in incompressible viscous fluid for very large Reynolds numbers. In: Doklady Akademii Nauk SSSR. vol. 30; 1941. p. 299–303.

[62] Durbin PA, Reif BP. Statistical theory and modeling for turbulent flows. John Wiley & Sons; 2011.

[63] Valen-Sendstad K, Mardal KA, Mortensen M, Reif BAP, Langtangen HP. Direct numerical simulation of transitional flow in a patient-specific intracranial aneurysm. Journal of Biomechanics. 2011;44(16):2826–2832.

[64] Reynolds O. An experimental investigation of the circumstances which determine whether the motion of water shall be direct or sinuous, and of the law of resistance in parallel channels. Proceedings of the Royal Society of London. 1883;35(224-226):84–99.

[65] Darbyshire A, Mullin T. Transition to turbulence in constant-mass-flux pipe flow. Journal of Fluid Mechanics. 1995;289:83–114.

[66] Faisst H, Eckhardt B. Sensitive dependence on initial conditions in transition to turbulence in pipe flow. Journal of Fluid Mechanics. 2004;504:343–352.

[67] Eckhardt B. Turbulence transition in pipe flow: 125th anniversary of the publication of Reynolds' paper. Philosophical Transactions of the Royal Society of London A: Mathematical, Physical and Engineering Sciences. 2009;367(1888):449–455.

[68] Eckhardt B. Turbulence transition in pipe flow: some open questions. Nonlinearity. 2007;21(1):T1.

[69] Pfenninger W. Boundary layer suction experiments with laminar flow at high reynolds numbers in the Inlet length of a tube by various

suction methods. In: Lachmann GV, editor. Boundary Layer and Flow Control. Pergamon; 1961. p. 961–980.

[70] Hof B, Juel A, Mullin T. Scaling of the turbulence transition threshold in a pipe. Physical Review Letters. 2003;91(24):244502.

[71] Peixinho J, Mullin T. Finite-amplitude thresholds for transition in pipe flow. Journal of Fluid Mechanics. 2007;582:169–178.

[72] Shan H, Zhang Z, Nieuwstadt F. Direct numerical simulation of transition in pipe flow under the influence of wall disturbances. International Journal of Heat and Fluid Flow. 1998;19(4):320–325.

[73] Meseguer A. Streak breakdown instability in pipe Poiseuille flow. Physics of Fluids (1994-present). 2003;15(5):1203–1213.

[74] Eckhardt B, Mersmann A. Transition to turbulence in a shear flow. Physical Review E. 1999;60(1):509–517.

[75] Mullin T, Peixinho J. Recent observations of the transition to turbulence in a pipe. In: IUTAM Symposium on Laminar-turbulent Transition. Springer; 2006. p. 45–55.

[76] Box GE, Draper NR. Empirical model-building and response surfaces. vol. 424. Wiley New York; 1987.

[77] Steinman DA, Kehoe SC, Ford MD, Nikolov HN, Holdsworth DW. Dancing on the knife-edge of symmetry: on the misuse of symmetric models for studying blood flow dynamics. In: Proceedings of ASME 2003 Summer Bioengineering Conference; 2003. p. 25–29.

[78] Varghese SS, Frankel SH, Fischer PF. Direct numerical simulation of stenotic flows. Part 1: steady flow. Journal of Fluid Mechanics. 2007;582:253–280.

[79] Varghese SS, Frankel SH, Fischer PF. Direct numerical simulation of stenotic flows. Part 2: pulsatile flow. Journal of Fluid Mechanics. 2007;582:281–318.

[80] Samuelsson J, Tammisola O, Juniper M. Breaking axi-symmetry in stenotic flow lowers the critical transition Reynolds number. Physics of Fluids (1994-present). 2015;27(10):104103.

[81] Griffith MD, Leweke T, Thompson MC, Hourigan K. Effect of small asymmetries on axisymmetric stenotic flow. Journal of Fluid Mechanics. 2013;721:R1.

[82] Ordsmith R. Pascal - an introduction to the art and science of programming. University Computing. 1988;10(3):164–164.

[83] Antiga L, Piccinelli M, Botti L, Ene-Iordache B, Remuzzi A, Steinman DA. An image-based modeling framework for patient-specific computational hemodynamics. Medical & Biological Engineering & Computing. 2008;46(11):1097–1112.

[84] Schroeder W, Martin K, Lorensen B. An Object-Oriented Approach To 3D Graphics. vol. 429. Prentice hall; 1997.

[85] Antiga L, Ene-Iordache B, Remuzzi A. Computational geometry for patient-specific reconstruction and meshing of blood vessels from MR and CT angiography. Medical Imaging, IEEE Transactions on. 2003;22(5):674–684.

[86] Attali D, Montanvert A. Computing and simplifying 2D and 3D continuous skeletons. Computer Vision and Image Understanding. 1997;67(3):261–273.

[87] Piccinelli M, Veneziani A, Steinman D, Remuzzi A, Antiga L, et al. A framework for geometric analysis of vascular structures: application to cerebral aneurysms. Medical Imaging, IEEE Transactions on. 2009;28(8):1141–1155.

[88] Aneurisk-Team. AneuriskWeb project website; 2012. Web Site. Available from: `http://ecm2.mathcs.emory.edu/aneuriskweb`.

[89] Passerini T, Sangalli LM, Vantini S, Piccinelli M, Bacigaluppi S, Antiga L, et al. An integrated statistical investigation of internal carotid arteries of patients affected by cerebral aneurysms. Cardiovascular Engineering and Technology. 2012;3(1):26–40.

[90] Bergersen A. Vmtktools; 2016. Accessed: 2016-15-03. Web Site. Available from: `https://github.com/aslakbergersen/vmtktools`.

[91] Ford M, Hoi Y, Piccinelli M, Antiga L, Steinman D. An objective approach to digital removal of saccular aneurysms: technique and applications. The British Journal of Radiology. 2009;82:S55–S61.

[92] Hanson AJ, Ma H. Parallel transport approach to curve framing. Indiana University, Techreports-TR425. 1995;11:3–7.

[93] Bogunović H, Pozo JM, Cárdenes R, Villa-Uriol MC, Blanc R, Piotin M, et al. Automated landmarking and geometric characterization of the carotid siphon. Medical Image Analysis. 2012;16(4):889–903.

[94] Tütüncü F, Schimansky S, Baharoglu MI, Gao B, Calnan D, Hippelheuser J, et al. Widening of the basilar bifurcation angle: association with presence of intracranial aneurysm, age, and female sex: clinical article. Journal of Neurosurgery. 2014;121(6):1401–1410.

[95] Seshadhri S, Janiga G, Beuing O, Skalej M, Thévenin D. Impact of stents and flow diverters on hemodynamics in idealized aneurysm models. Journal of Biomechanical Engineering. 2011;133(7):071005.

[96] Hoi Y, Wasserman BA, Xie YJ, Najjar SS, Ferruci L, Lakatta EG, et al. Characterization of volumetric flow rate waveforms at the carotid bifurcations of older adults. Physiological Measurement. 2010;31(3):291–302.

[97] Valen-Sendstad K, Piccinelli M, KrishnankuttyRema R, Steinman DA. Estimation of inlet flow rates for image-based aneurysm CFD models: where and how to begin? Annals of Biomedical Engineering. 2015;43(6):1422–1431.

[98] Alastruey J, Parker K, Peiró J, Byrd S, Sherwin S. Modelling the circle of Willis to assess the effects of anatomical variations and occlusions on cerebral flows. Journal of Biomechanics. 2007;40(8):1794–1805.

[99] Lee SW, Antiga L, Steinman DA. Correlations among indicators of disturbed flow at the normal carotid bifurcation. Journal of Biomechanical Engineering. 2009;131(6):061013.

[100] Wiebers DO, International Study of Unruptured Intracranial Aneurysms Investigators and others. Unruptured intracranial aneurysms: natural history, clinical outcome, and risks of surgical and endovascular treatment. The Lancet. 2003;362(9378):103–110.

[101] Zeng Z, Kallmes DF, Durka M, Ding Y, Lewis D, Kadirvel R, et al. Hemodynamics and anatomy of elastase-induced rabbit aneurysm models: similarity to human cerebral aneurysms? American Journal of Neuroradiology. 2011;32(3):595–601.

[102] Sato K, Ogoh S, Hirasawa A, Oue A, Sadamoto T. The distribution of blood flow in the carotid and vertebral arteries during dynamic exercise in humans. The Journal of Physiology. 2011;589(11):2847–2856.

[103] Querido JS, Sheel AW. Regulation of cerebral blood flow during exercise. Sports Medicine. 2007;37(9):765–782.

[104] Westerhof N, Stergiopulos N, Noble MI. Snapshots of hemodynamics: an aid for clinical research and graduate education. Springer Science & Business Media; 2010.

[105] Valen-Sendstad K. On the assumption of laminar flow in the cerebrovasculature: Implications for CFD insights into aneurysm initiation and rupture?; 2015. .

[106] Murray CD. The physiological principle of minimum work I. The

vascular system and the cost of blood volume. Proceedings of the National Academy of Sciences. 1926;12(3):207–214.

[107] Cebral J, Castro M, Putman C, Alperin N. Flow–area relationship in internal carotid and vertebral arteries. Physiological Measurement. 2008;29(5):585–594.

[108] Marinkovic S, Milisavljevic M, Kovacevic M, Stevic Z. Perforating branches of the middle cerebral artery. Microanatomy and clinical significance of their intracerebral segments. Stroke. 1985;16(6):1022–1029.

[109] Valencia A, Solis F. Blood flow dynamics and arterial wall interaction in a saccular aneurysm model of the basilar artery. Computers & Structures. 2006;84(21):1326–1337.

[110] Cebral J, Hendrickson S, Putman C. Hemodynamics in a lethal basilar artery aneurysm just before its rupture. American Journal of Neuroradiology. 2009;30(1):95–98.

[111] Khan S, Cloud G, Kerry S, Markus HS. Imaging of vertebral artery stenosis: a systematic review. Journal of Neurology, Neurosurgery & Psychiatry. 2007;78(11):1218–1225.

[112] Stehbens WE, Stehbens GR. Flow in glass models simulating vascular junctions under steady flow conditions. Quarterly Journal of Experimental Physiology. 1985;70(4):515–526.

[113] Lauric A, Safain MG, Hippelheuser J, Malek AM. High curvature of the internal carotid artery is associated with the presence of intracranial aneurysms. Journal of Neurointerventional Surgery. 2014;6(10):733–739.

[114] Silva Neto ÂR, Câmara RLB, Valença MM. Carotid siphon geometry and variants of the circle of Willis in the origin of carotid aneurysms. Arquivos de Neuro-psiquiatria. 2012;70(12):917–921.

[115] Lee K, Parker K, Caro C, Sherwin S. The spectral/HP element modelling of steady flow in non-planar double bends. International Journal for Numerical Methods in Fluids. 2008;57(5):519–529.

[116] Stehbens WE. Pathology of the cerebral blood vessels. CV Mosby; 1972.

[117] Davies PF. Hemodynamic shear stress and the endothelium in cardiovascular pathophysiology. Nature Clinical Practice Cardiovascular Medicine. 2009;6(1):16–26.

[118] Davies PF, Remuzzi A, Gordon EJ, Dewey CF, Gimbrone MA. Turbulent fluid shear stress induces vascular endothelial cell turnover

in vitro. Proceedings of the National Academy of Sciences. 1986;83(7):2114–2117.

[119] Ignarro LJ, Buga GM, Wood KS, Byrns RE, Chaudhuri G. Endothelium-derived relaxing factor produced and released from artery and vein is nitric oxide. Proceedings of the National Academy of Sciences. 1987;84(24):9265–9269.

[120] Arkenbout EK, Dekker RJ, de Vries CJ, Horrevoets AJ, Pannekoek H, et al. Focusing on transcription factor families in atherogenesis: the function of LKLF and TR3. Thrombosis and Haemostasis. 2003;89(3):522–529.

[121] Wang N, Miao H, Li YS, Zhang P, Haga JH, Hu Y, et al. Shear stress regulation of Krüppel-like factor 2 expression is flow pattern-specific. Biochemical and Biophysical Research Communications. 2006;341(4):1244–1251.

[122] Yamamoto K, Protack CD, Kuwahara G, Tsuneki M, Hashimoto T, Hall MR, et al. Disturbed shear stress reduces Klf2 expression in arterial-venous fistulae in vivo. Physiological Reports. 2015;3(3):e12348.

[123] Seok J, Warren HS, Cuenca AG, Mindrinos MN, Baker HV, Xu W, et al. Genomic responses in mouse models poorly mimic human inflammatory diseases. Proceedings of the National Academy of Sciences. 2013;110(9):3507–3512.

[124] Weinberg PD, Ethier CR. Twenty-fold difference in hemodynamic wall shear stress between murine and human aortas. Journal of Biomechanics. 2007;40(7):1594–1598.

[125] Marzo A, Singh P, Larrabide I, Radaelli A, Coley S, Gwilliam M, et al. Computational hemodynamics in cerebral aneurysms: the effects of modeled versus measured boundary conditions. Annals of Biomedical Engineering. 2011;39(2):884–896.

[126] Xiang J, Tremmel M, Kolega J, Levy EI, Natarajan SK, Meng H. Newtonian viscosity model could overestimate wall shear stress in intracranial aneurysm domes and underestimate rupture risk. Journal of Neurointerventional Surgery. 2011;p. neurintsurg–2011.

[127] Castro MA, Olivares MCA, Putman CM, Cebral JR. Unsteady wall shear stress analysis from image-based computational fluid dynamic aneurysm models under Newtonian and Casson rheological models. Medical & Biological Engineering & Computing. 2014;52(10):827–839.

[128] Isaksen JG, Bazilevs Y, Kvamsdal T, Zhang Y, Kaspersen JH, Water-

loo K, et al. Determination of wall tension in cerebral artery aneurysms by numerical simulation. Stroke. 2008;39(12):3172–3178.

[129] Bazilevs Y, Hsu MC, Zhang Y, Wang W, Kvamsdal T, Hentschel S, et al. Computational vascular fluid–structure interaction: methodology and application to cerebral aneurysms. Biomechanics and Modeling in Mechanobiology. 2010;9(4):481–498.

[130] Peng L, Nielsen PV, Wang X, Sadrizadeh S, Liu L, Li Y. Possible User-Dependent CFD Predictions of Transitional Flow in Building Ventilation. Building and Environment. 2016;.

[131] Steinman DA, Hoi Y, Fahy P, Morris L, Walsh MT, Aristokleous N, et al. Variability of computational fluid dynamics solutions for pressure and flow in a giant aneurysm: the ASME 2012 Summer Bioengineering Conference CFD Challenge. Journal of Biomechanical Engineering. 2013;135(2):021016.

[132] Valen-Sendstad K. The 2015 aneurysm CFD challenge: variability of segmentations, hemodynamics, and hemodynamic indices: qualitative and preliminary results; 2015. Summer Biomechanics, Bioengineering & Biotransport Conference, Utah, USA, 2015.